Astronomy & Astrophysics manuscript no. paper_M4
February 6, 2017

Atomic diffusion and mixing in old stars VII: Chemical abundance variations in M4 (NGC 6121)⋆⋆⋆

Thomas Nordlander[1], Pieter Gruyters[1,2], Olivier Richard[3], and Andreas J. Korn[1]

[1] Division of Astronomy and Space Physics, Department of Physics and Astronomy, Uppsala University, Box 516, 75120 Uppsala, Sweden
[2] Lund Observatory, Box 43, 221 00 Lund, Sweden
[3] LUPM, Université de Montpellier, CNRS, CC072, Place E. Bataillon, 34095 Montpellier Cedex, France

Received / Accepted

ABSTRACT

Context. Variations in chemical abundances with evolutionary phase have been identified in previous papers of this series among stars in three globular clusters, M30 ([Fe/H] = −2.3), NGC 6397 ([Fe/H] = −2.1) and NGC 6752 ([Fe/H] = −1.6). These variations compare well with the predictions from stellar-structure models with atomic diffusion moderated by additional mixing of low and high efficiency at the respective ends of the metallicity scale.
Aims. By extending these studies to higher metallicity, for a large number of elements, further empirical constraints can be provided to the nature of the additional mixing mechanism. We therefore investigate whether evolutionary abundance variations are present among stars in the globular cluster NGC 6121 (M4, [Fe/H] = −1.1).
Methods. We perform a detailed chemical abundance analysis of 86 stars, ranging from the cluster turnoff point to the red giant branch just above the bump. We determine the abundances of 14 elements consistently by means of spectrum matching, using medium-resolution spectra obtained with VLT/FLAMES-GIRAFFE. Stellar parameters are obtained from $UBVI$ broadband photometry, after correcting for differential reddening effects.
Results. We observe the usual C-N-O anticorrelations and confirm the presence of a bimodal population characterised by their N content. We find systematic evolutionary variations in individual chemical abundances of weak statistical significance, but which are rather robust to uncertainties in stellar parameters and modelling assumptions, for magnesium, silicon, calcium, titanium and iron. These variations match predictions from stellar evolution models including atomic diffusion if efficient additional mixing is employed, in line with previous results. Using these models, we derive an initial lithium abundance for the cluster, 2.59 ± 0.10, which is fully compatible with those determined for M30, NGC 6397 and NGC 6752, falling slightly short of the predicted primordial BBN value.
Conclusions. The observed abundance patterns of 14 elements investigated here suggest that the second generation stars in M4 were formed out of gas that was polluted by both massive (20–40 $M_\odot$) stars and AGB stars. Element-specific abundance trends are identified in stars along the evolutionary sequence in M4. Although the significance of the individual trends is weak, they all seem to indicate that atomic diffusion is at work in M4. This is the fourth cluster in which atomic diffusion signatures are seen, giving more evidence for the assumption that atomic diffusion produces measurable surface-abundance changes in warm metal-poor stars and hence should be accounted for in stellar-evolution models and studies of Galactic chemical evolution.

Key words. stars: abundances - stars: atmospheres - stars: fundamental parameters - globular cluster and associations: M4 - techniques: spectroscopic

1. Introduction

The chemical evolution of the Milky Way is believed to be imprinted in the elemental abundance patterns of late-type stars (spectral types F to K). Due to their long lifetimes, these stars are of particular importance when it comes to studying the build-up of elements during the early times of our Galaxy. The chemical composition of the atmospheric layers of such stars is thought to resemble the gas from which they were formed. However, recent observations in globular clusters (GCs) have shown a somewhat more complicated picture. Not only did recent spectroscopic studies reveal a spread in the abundance of light elements in stars of all GCs (Gratton et al. 2012, and references therein), the studies also indicate that there are processes at work in these stars which alter their surface composition. These element-separating effects are collectively referred to as atomic diffusion (Michaud et al. 1984). The effects are responsible for an exchange of material between the star's interior and its atmosphere during the main sequence lifetime of the star but can be largely counteracted as long as convection is efficient. This means that the largest surface effects are expected for the hotter stars in an old stellar population, i.e., the F-type turnoff-point (TOP) stars. As the stars evolve off the main sequence (MS), the deepening outer convection zone restores the original surface composition and washes out the diffusion effects. At the TOP, layers below the outer convection zone are however sufficiently hot to partially destroy lithium. As the convection zone deepens, the surface layers are thus diluted by lithium-depleted material, causing the surface lithium abundance to drop by an order of magnitude.

Driven by the theoretical modelling work by Michaud et al. (1984) and more recently by Richard et al. (2002a,b, 2005), the observational search for evidence of atomic diffusion in Popu-

Send offprint requests to: Thomas.Nordlander@physics.uu.se
⋆ Based on data collected at the ESO telescopes under program 081.D-0356.
⋆⋆ The figures are available in colour in the electronic form.

lation II stars began. A series of papers gives an overview of the abundance analyses of unevolved and evolved stars in the GCs NGC 6397 (Korn et al. 2007; Lind et al. 2008; Nordlander et al. 2012), NGC 6752 (Gruyters et al. 2013, 2014), and M30 (Gruyters et al. 2016) at metallicities [Fe/H][1] = −2.1, [Fe/H] = −1.6, and [Fe/H] = −2.3, respectively. The analyses revealed element-specific abundance differences of 0.1–0.3 dex between stars on the TOP and on the red giant branch (RGB). These abundance trends are remarkably similar to the ones predicted by stellar evolution models including atomic diffusion for Population II stars.

However, the observations are not matched by the predictions of atomic diffusion based on calculations from first principles. To achieve agreement, the effect of atomic diffusion needs to be moderated by an unknown physical mechanism providing additional mixing (AddMix). This non-canonical mixing beyond the formal extent of the convection zone is also needed to explain the properties of the Spite plateau of lithium (Spite & Spite 1982) which shows a constant Li abundance in unevolved, Population II stars (Richard et al. 2002b, 2005). The additional mixing is incorporated in the stellar evolution models in an ad-hoc parameterisation (Richer et al. 2000) so that the structure of the model star is modified by mixing a certain depth range. The density dependence (ρ^{-3}) is suggested by the Be abundance on the Sun (Proffitt & Michaud 1991). The free parameter is the logarithm of a reference temperature T_0 which sets the overall efficiency of the AddMix (see Richer et al. 2000, for the analytic expression of the coefficient). With this parameterisation, Richard et al. (2005) were able to reproduce the Spite plateau using a range of models from T6.0 to T6.28 (T6.28 is shorthand for models where $\log T_0 = 6.28$). These are also the models explored in this series of papers where we find that the abundance trends in M30 at [Fe/H] = −2.3 and NGC 6397 at [Fe/H] = −2.1 are best reproduced by the T5.8 and T6.0 models, respectively, while in NGC 6752 at [Fe/H] = −1.6 the T6.2 models are in best agreement with the observed abundance trends. In all three cases we find diffusion-corrected Li abundances which are compatible with predictions of standard Big-Bang Nucleosynthesis (BBN) based on observations of the cosmic microwave background radiation (CMB) by the *Wilkinson Microwave Anisotropy Probe* (WMAP) and Planck, $\log \epsilon(\mathrm{Li}) = 2.67 \pm 0.07$ (Cyburt et al. 2016). We note that other recent analyses yield statistically equivalent values in the range 2.69–2.72 (e.g., Coc et al. 2013; Anders et al. 2014; Nollett & Steigman 2014). Given these results, it seems that the efficiency of AddMix is metallicity-dependent. To investigate the validity of this hypothesis we here investigate abundance variations in NGC 6121, also known at M4, at [Fe/H] = −1.1.

Located at a distance of 1.8 kpc (Hendricks et al. 2012), M4 is the nearest GC to the Sun. As M4 is a bright and well populated GC, but is located at low Galactic latitude, in the Galactic disk behind the Sco-Oph cloud complex, and thus suffers from significant interstellar extinction ($A_V = 1.39$, Hendricks et al. 2012) and strong spatial differential reddening (Cudworth & Rees 1990; Drake et al. 1994; Ivans et al. 1999). Deriving effective temperatures ($T_{\rm eff}$) from photometry thus becomes a cumbersome task. Recent studies in the literature include Marino et al. (2008, 2011), who presented evidence for multiple populations along the RGB and horizontal branch (HB), Spite et al. (2016) who did the same for stars on the TOP and SBG, and Monelli et al. (2013) who demonstrated the presence of two distinct sequences on the RGB. Other high-resolution spectroscopic studies have derived abundances for RGB stars, e.g., the lithium content of RGB stars was studied by D'Orazi et al. (2010) and Monaco et al. (2012).

Table 1. Recent metallicity determinations of M4.

Reference	[Fe/H]	# stars	Sample
Marino et al. (2008)	−1.07	105	RGB
Mucciarelli et al. (2011)	−1.10	87	TOP to RGB
Monaco et al. (2012)	−1.31	71	MS
Monaco et al. (2012)	−1.17	10	SGB/RGB
Malavolta et al. (2014)	−1.16	1869	MS/SGB
Malavolta et al. (2014)	−1.07	332	SGB/RGB
Spite et al. (2016)	−1.20	71	TOP
Spite et al. (2016)	−1.10	10	SGB

More recently, M4 has been the topic of a controversy concerning the absence or presence of second-generation stars on the asymptotic giant branch (AGB). MacLean et al. (2016) analysed high-resolution spectra of 106 RGB and 15 AGB stars and concluded that there are no second generation stars among the AGB stars. In contrast, Lardo et al. (2016) showed using the $C_{UBI} = (U - B) - (B - I)$ photometric index, that the AGB is in fact also composed of two stellar populations.

The atomic diffusion effects on Fe and Li along the evolutionary sequence in M4 has previously been addressed by Mucciarelli et al. (2011). Although the literature on M4 reveals a tendency that Fe abundances are generally lower for TOP than RGB stars (see Table 1), Mucciarelli et al. (2011) did not find an evolutionary trend in Fe with $T_{\rm eff}$. Their results do, however, indicate the need for atomic diffusion with very efficient AddMix in order to explain the observed evolution of Li in the cluster. Given the small size of the expected atomic diffusion trends for Fe and the temperature-sensitivity of Fe I lines, it is not unlikely that the atomic diffusion effect on Fe may go undetected. As atomic diffusion affects all elements, we here revisit M4 and derive abundances for 14 elements, to determine whether atomic diffusion signatures are present. In particular, for 10 elements our analysis takes into account departures from LTE (non-LTE, or NLTE), and we use lines of the ionised species in our analysis of Ti and Fe which are known to be rather immune to both NLTE and 3D effects.

This paper is organized as follows: The observational data are summarised in Sect. 2. In Sect. 3 we outline the derivation of the stellar parameters and discuss our methodology. The results are presented in Sect. 4 followed by a scientific discussion in Sect. 5. We conclude the paper with a summary in Sect. 6.

2. Observations

The abundance analysis in this work is based on high-resolution spectroscopic observations of 86 stars in M4 presented by Lovisi et al. (2010) and previously used by Mucciarelli et al. (2011, hereafter Mu2011). We obtained reduced spectroscopic data from the Paris-GIRAFFE archive (Royer et al. 2012). The observations were carried out using the multi-object spectrograph FLAMES/GIRAFFE mounted on the ESO VLT-UT2 Kueyen (Pasquini et al. 2003). All stars have been observed with the HR15N, HR18 and HR22A settings (centered on wavelengths of 6650, 7691, and 9205 Å) within the framework of the search for anomalous abundances in Blue Straggler Stars (see Ferraro et al. 2006). The stars cover a range in evolution from the TOP

[1] We adopt here the customary spectroscopic notations that $[X/Y] \equiv \log(N_X/N_Y)_* - \log(N_X/N_Y)_\odot$, and that $\log \varepsilon(X) \equiv \log(N_X/N_H) + 12$ for elements X and Y.

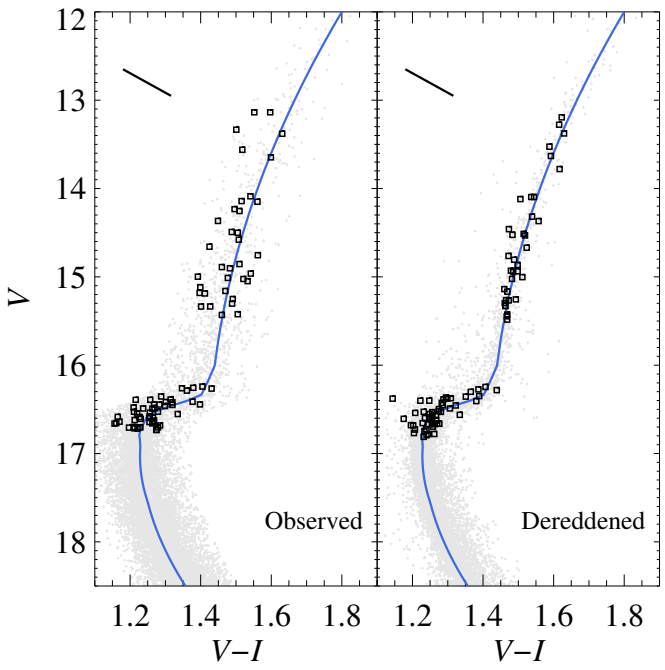

Fig. 1. Observed $(V-I)$–V colour-magnitude diagram of M4 before and after correcting for differential reddening. The spectroscopic targets are marked by black squares. The reddening vector is given by the solid line in the top left corner. The solid blue line indicates the fiducial sequence.

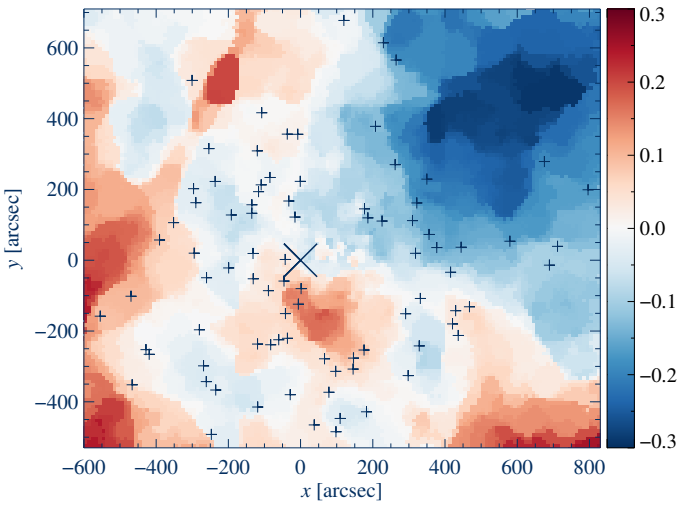

Fig. 2. Observed $(V-I)$–V reddening map of M4, indicating variations in extinction, ΔA_V, relative to the cluster average. Spectroscopic targets are marked by black crosses, while X marks the center of the cluster. The blue colour indicates areas with less reddening, while red coloured areas are affected by a higher degree of reddening. The coordinate system is normalised to the cluster centre at R.A. = $16^{\rm h}26^{\rm m}45.12^{\rm s}$, Dec = $26°18'35\farcs4$.

to the RGB and are shown in the $(V-I)$–V colour magnitude diagram (CMD) in Fig. 1. Reduced broadband $UBVI$ photometry of M4 was kindly provided by Y. Momany (priv. comm.). Further information is given by Momany et al. (2003), and the same photometry was previously used by Marino et al. (2008).

3. Analysis

3.1. Photometry

The line of sight towards M4 is heavily affected by interstellar dust due to its location behind the Sco-Oph cloud complex. This results in a large amount of global reddening ($E(B-V) = 0.37$ Hendricks et al. 2012), strong V-band extinction ($A_V = 1.39$ Hendricks et al. 2012), and significant differential reddening across the face of the cluster (Ivans et al. 1999). Estimates of the peak-to-peak variation within a distance of 10′ of the cluster centre range from $\delta E(B-V) \geqslant 0.05$ (Cudworth & Rees 1990) to $\delta E(B-V) = 0.25$ (Mu2011).

The effect of differential reddening is an apparently broader evolutionary sequence in the cluster CMD than expected from photometric uncertainties alone. Moreover, this broadening will depend on the angle between the sequence and the reddening vector, which is the ratio between total and selective extinction, e.g., $A_V/E(V-I)$. The larger the angle between vector and sequence, the larger the scatter will appear to be. This is illustrated in Fig. 1, which shows the cluster $(V-I)$–V CMD before and after dereddening. To correct for the spatially differential reddening across the face of the cluster, a fiducial sequence was determined by eye. The selective extinction in $(V-I)$ was derived by matching this fiducial to a 12 Gyr isochrone computed with a chemical composition appropriate for the cluster, where $Y = 0.25$, [Fe/H] $= -1.1$, and [α/Fe] $= +0.4$, using the Montréal-Montpellier stellar evolution code which includes atomic diffusion (Richard et al. 2002b). The matching was performed in V–$T_{\rm eff}$ space, and we use the photometric calibrations for $V-I$ from Ramírez & Meléndez (2005), which are calibrated on the infrared flux method (IRFM, Blackwell et al. 1986). The difference between the $T_{\rm eff}$–V sequence and the isochrone indicated the selective extinction $E(V-I) = 0.63$.

A reference sample of stars was constructed by computing the distance along the reddening vector to the fiducial sequence for all stars located near the main-sequence turnoff point, $16.7 \leq V \leq 18.3$. For each star in the photometric catalogue, we determined the average reddening by median filtering amongst the nearest ≤ 35 neighbouring reference stars within a distance of 60″ on the sky. The differential extinction relative to the average cluster extinction, ΔA_V, as derived empirically from the comparison to $(V-I)$–V fiducial sequences is illustrated in Fig. 2 where red (blue) colours indicate stronger (weaker) reddening than the average. The illustration has been binned to cells of 10″ by 10″, each of which represents the median ΔA_V of all stars that fall in the coordinate range and for which a reddening value has been assigned by the method described above. The map is qualitatively consistent with the $(B-V)$ reddening map published in Hendricks et al. (2012) and Monelli et al. (2013).

A corresponding dereddening map based on the $(B-I)$ colour index was also derived. As Ramírez & Meléndez (2005) do not provide a $(B-I)$–$T_{\rm eff}$ transformation, the Hendricks et al. (2012) transformation factors (see their Table 3) were used to obtain $E(B-I) = 1.06$ from our derived value of $E(V-I) = 0.63$. The $(B-I)$ reddening map is qualitatively similar to that derived from $(V-I)$. The influence of the differences between the two reddening maps on derived stellar parameters will be examined further in Sect. 3.3. The excellent agreement between the two reddening maps, and the significantly decreased scatter along the RGB in Fig. 1 validates the accuracy of the dereddening procedure.

3.2. Spectrum synthesis

We performed an automated spectroscopic analysis similar to the analysis presented in Gruyters et al. (2014), and apply the tools developed for that analysis. Briefly, stellar parameters ($T_{\rm eff}$, $\log g$, [Fe/H] and $v_{\rm mic}$), linelists (Piskunov et al. 1995; Kupka et al. 1999), and line and continuum masks are supplied to a modified version of the spectrum synthesis code Spectroscopy Made Easy (SME, Valenti & Piskunov 1996; Valenti & Fischer 2005; Piskunov & Valenti 2016). The code allows for non-LTE (NLTE) line formation and uses a grid of MARCS plane-parallel and spherically symmetric model atmospheres (Gustafsson et al. 2008), all with scaled solar abundances and alpha-enhancement of 0.4 dex when [Fe/H] < -1. SME computes spectra on the fly, and performs a non-linear optimisation fitting synthetic to observed spectra (Marquardt 1963; Press et al. 1992). Rather than a line-by-line approach, we determine all abundances simultaneously by synthesising all three spectral settings for each star. This ensures a consistent abundance table for each star, where all known line blends are explicitly taken into account.

3.3. Photometric stellar parameters

A photometric effective-temperature ($T_{\rm eff}$) scale was constructed by transforming $(V-I)$ colours using the relations from Ramírez & Meléndez (2005). The calibrations are applied assuming [Fe/H] $= -1.1$ for all stars, after dereddening the $(V-I)$ colours of individual stars and placing them on the fiducial sequence.

We evaluate the uncertainty of the dereddened colours by comparing results using the independent $(V-I)$ and the $(B-I)$ reddening maps. Differences are small, 7 ± 34 K and 10 ± 73 K for giants and dwarfs, respectively. The scatter about the $(V-I)$ fiducial sequence is 45 and 135 K, for giants and dwarfs. The median absolute deviation from the nearest neighbour filtering is just 0.032 mag in V, corresponding to 0.015 mag in $(V-I)$. The latter corresponds to a change in $T_{\rm eff}$ of 36 and 68 K for giants and dwarfs, respectively. We find good agreement between these different error estimates, and therefore adopt representative uncertainties of 50 and 100 K in $T_{\rm eff}$ for giants and dwarfs, respectively.

Compared to the $T_{\rm eff}$ scale of Mu2011, results are in agreement for turnoff stars (our temperatures are higher by 17 ± 129 K for stars where $T_{\rm eff} > 5800$ K), while the values for giants ($T_{\rm eff} < 5200$ K) differ by -58 ± 21 K. Large differences are found on the SGB (intermediate $T_{\rm eff}$), -115 ± 121 K.

Photometric surface gravities are derived from the position of the stars in the CMD and assuming a distance modulus of 11.28 (Hendricks et al. 2012). The bolometric corrections of Alonso et al. (1999, 2001) are applied to dereddened V magnitudes, as a function of metallicity and $T_{\rm eff}$, to compute luminosities. Stellar masses are interpolated as a function of $T_{\rm eff}$ from a 12 Gyr isochrone, and range from 0.84 to 0.87 $M_\odot$. The resulting values of $\log g$ range from 4.2 at $T_{\rm eff} = 6100$ K (TOP) to 2.2 at $T_{\rm eff} = 4700$ K (RGB). Photometric observational data and stellar parameters are given in Table 2.

As outlined in Gruyters et al. (2014), uncertainties in $T_{\rm eff}$ are expected to dominate relative errors in $\log g$. For example, an error of +100 K in $T_{\rm eff}$ translates into +0.03 dex in $\log g$. An effect of this size on $\log g$ would require, e.g., an increase in stellar mass by 0.06 $M_\odot$, or an increase in V magnitude by 0.075 mag. Our expected precision of 0.03 mag in V magnitude and 50 and 100 K in $T_{\rm eff}$ for giants and dwarfs, respectively, thus translates into relative uncertainties in $\log g$ by at most 0.03 and 0.05 dex for giants and dwarfs, respectively.

3.4. Spectroscopic stellar parameters

3.4.1. Microturbulence

Microturbulent velocities are derived from a set of 17 Fe I lines, since the spectra contain only two (rather weak) Fe II lines. The Fe I lines span a range in equivalent widths of 20–150 mÅ ($\log W_\lambda/\lambda = -5.5$ to -4.6) and 5–80 mÅ (-6.5 to -4.9) for the coolest and hottest stars in our sample.

We find that dwarfs follow an essentially linear relation of $v_{\rm mic}$ increasing with $T_{\rm eff}$, while giants exhibit $v_{\rm mic}$ values decreasing linearly with $\log g$. The RMS scatter about the linear relation for giant stars is just 0.048 km s^{-1}, while that for the dwarfs is considerably higher and amounts to 0.43 km s^{-1}. Among the 20 hottest TOP stars ($T_{\rm eff} > 6080$ K), which are the faintest and thus exhibit the lowest S/N values, we find a scatter of 0.8 km s^{-1}, and values higher than 3 km s^{-1} in several stars. This indicates that we cannot robustly determine $v_{\rm mic}$ for all stars in our sample.

To alleviate this shortcoming, we analyse coadded spectra, generated by grouping stars according to their stellar parameters. The characteristics of each group-averaged spectrum are given in Table 3. For giant stars, these $v_{\rm mic}$ values follow a similar relation to those determined from individual stars, where their slopes as a function of $\log g$ agree to within 1σ, indicating that the approach is viable. For dwarfs, we find a linear relation as a function of $T_{\rm eff}$ with a scatter of just 0.075 km s^{-1}. Adopting the two relations leads to $v_{\rm mic}$ values ranging between 1.2 and 1.7 km s^{-1} for the dwarfs ($T_{\rm eff} > 5500$ K) while the giants ($T_{\rm eff} < 5500$ K, $\log g < 3.8$) have lower $v_{\rm mic}$ values between 1.1 and 1.5 km s^{-1}.

3.4.2. Spectroscopic $T_{\rm eff}$ scales

Preliminary results for the iron abundances derived from lines of Fe I and Fe II reveal a potential problem with the photometric stellar parameters. In the giants, iron abundances derived from Fe I lines appear to correlate with effective temperature. Abundances in the coolest stars ($T_{\rm eff} < 5000$ K) from Fe I lines are lower than those from Fe II lines by 0.04 dex. The warmer giants, subgiants and dwarfs exhibit better agreement between the abundance indicators, with a possible bias of lower abundances of Fe I than Fe II by 0.03 dex. Previous analyses of UVES and GIRAFFE spectra of stars in this cluster using photometric stellar parameters (Carretta et al. 2009a,b) found that the average abundances determined from Fe I and Fe II lines agreed to within 0.003 dex. Such remarkably good agreement is curious, given that their analysis was based on 1D LTE synthesis.

The abundances we derive from lines of Fe II are found to be in very good agreement with predictions from evolutionary models, as shown in Fig. 3. The abundance trend in titanium as deduced from a Ti II line is likewise in very good agreement with predictions. Lines of ionised iron and titanium are known to form under conditions close to LTE, with very small sensitivity to hydrodynamical effects (see Sect. 3.7), and are rather insensitive to changes in $T_{\rm eff}$. Our small estimated uncertainties in $\log g$ and the weak sensitivity to $v_{\rm mic}$ likewise indicate these results to be robust. We thus suspect that the uncovered deviation from ionisation equilibrium is due to inaccuracies in the temperature scale, which the lines of Fe I are susceptible to.

The wings of the broad Hα line are commonly used in the literature, and are known to yield accurate stellar parameters (Barklem et al. 2002; but, see also Ludwig et al. 2009). However, the sensitivity of these lines decreases significantly on the RGB, where Mucciarelli et al. (2011) estimated uncertainties of

Table 2. Dereddened photometry, S/N of the spectroscopic material and photometric stellar parameters.

ID	RA (J2000)	Dec (J2000)	$V-I$ (mag)	V (mag)	S/N	$T_{\rm eff}$ (K)	$\log g$ (dex)	$v_{\rm mic}$ (km s^{-1})
M4-8460	245.9471893	-26.3749981	1.512	14.507	120	4970	2.84	1.32
M4-8777	245.9373932	-26.3614750	1.462	15.257	95	5057	3.18	1.24
M4-9156	245.9069977	-26.3439293	1.539	14.083	115	4888	2.64	1.37
M4-13282	245.7902069	-26.3910408	1.238	16.582	51	5923	4.04	1.53
M4-28007	245.8050232	-26.6688786	1.504	14.949	93	5051	3.04	1.28

Notes. The full table can be retrieved from CDS/Vizier.

Table 3. Photometric stellar parameter selection and average photometric stellar parameters for the coadded group-averaged spectra.

Group	# stars	S/N	$T_{\rm eff}$-range (K)	$\log g$-range (dex)	Mean $T_{\rm eff}$ (K)	Mean $\log g$ (dex)
RGB1	6	208	4692–4814	2.18–2.43	4747 ± 47	2.31 ± 0.10
RGB2	18	308	4868–5074	2.64–3.08	4975 ± 60	2.88 ± 0.15
RGB3	11	267	5001–5112	3.15–3.28	5078 ± 36	3.21 ± 0.05
SGB1	2	81	5454–5523	3.76–3.81	5489 ± 48	3.78 ± 0.03
SGB2	3	86	5620–5683	3.87–3.92	5642 ± 35	3.89 ± 0.02
SGB3	7	122	5730–5815	3.89–3.98	5773 ± 37	3.93 ± 0.03
TOP1	10	142	5824–5908	3.98–4.08	5868 ± 27	4.03 ± 0.03
TOP2	10	129	5927–6021	3.97–4.14	5984 ± 34	4.08 ± 0.05
TOP3	14	137	6041–6572	4.02–4.20	6212 ± 152	4.13 ± 0.06

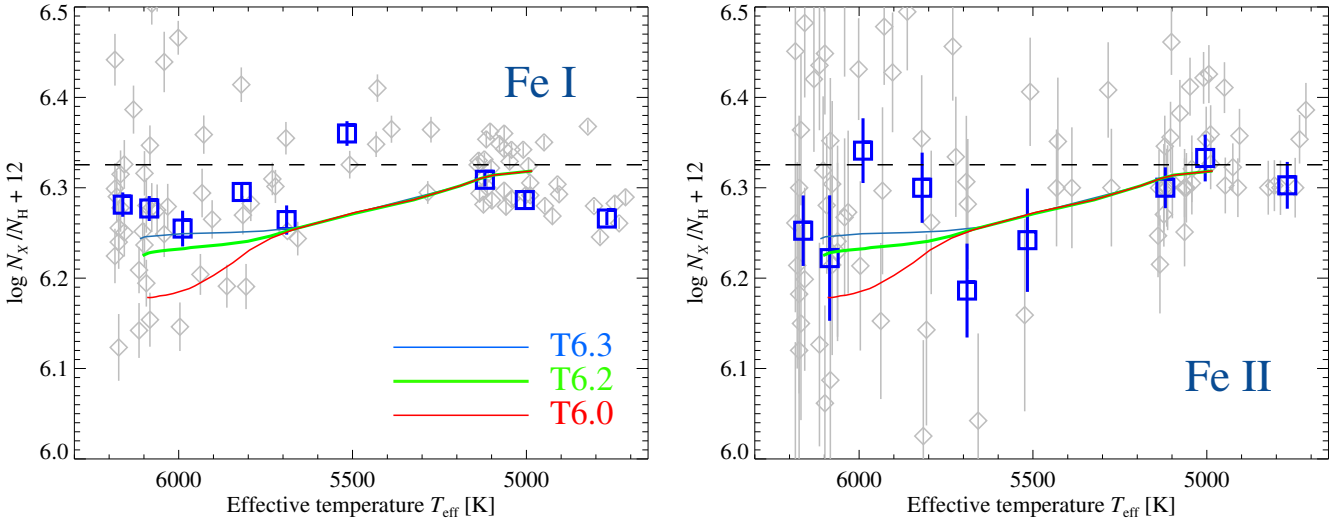

Fig. 3. Evolutionary abundance trends of iron derived from lines of Fe I (left) and Fe II (right) on the photometric $T_{\rm eff}$ scale. The blue squares represent abundances derived from the coadded group-averaged spectra, while abundances of the individual stars are shown as gray diamonds. Overplotted are predictions from stellar structure models including atomic diffusion with additional mixing of different efficiencies, at an age of 12 Gyr. Note the offset between Fe I and Fe II among the cooler stars, indicating that the ionisation balance is not fulfilled.

at least 300 K. While their analysis combined $T_{\rm eff}$ values determined using Hα for dwarfs with photometric temperatures on the RGB, we aim to make our analysis as homogeneous as possible to avoid possible systematic differences.

Our list of Fe I lines span the range of excitation energies between 2.5 and 4.5 eV, and should therefore be suitable to determine $T_{\rm eff}$ from the excitation equilibrium. However, we find that due to the limited number of lines and the limited quality of our spectra among the turnoff stars, differences compared to the photometric temperatures exhibit large scatter with individual differences as large as 550 K.

We therefore adopt an unusual method: we enforce the ionisation equilibrium by matching for each star the iron abundance based on Fe I lines, in NLTE, to the *average* Fe-trend deduced from coadded spectra using lines of Fe II. As this average trend is very similar to that predicted by stellar evolution models including atomic diffusion (AD) on the extreme ends of the temperature scale, where we have the largest number of stars to compare to, we adopt the predicted trend from a T6.2 model at each evolutionary stage. At low S/N, this fitting method is more robust than the excitation equilibrium. On average the resulting $T_{\rm eff}$ scale is cooler than the photometric by 80 ± 91 K, 104 ± 59 K and 29 ± 31 K for turnoff stars, subgiants, and giants, respectively.

To avoid circular arguments with respect to AD, we also generate a corresponding $T_{\rm eff}$ scale under the assumption that all stars must indicate the same iron abundance. This $T_{\rm eff}$ scale

is cooler than the photometric by 16 ± 75 K, 61 ± 60 K and 34 ± 29 K for dwarfs, subgiants and giants, respectively. Compared to the other spectroscopic temperature scale, this one differs by +65 ± 30, +44 ± 19 K and −5 ± 4 K for dwarfs, subgiants and giants, respectively. We will discuss the effect of the different $T_{\rm eff}$ scales on the inferred abundances in Sect. 5.3.

3.5. Deriving chemical abundances

We simultaneously determine the abundances of 14 elements, on each of the three $T_{\rm eff}$ scales discussed in Sects. 3.3 and 3.4.2. We analyse the light elements lithium using the Li I resonance line at 6707.8 Å, carbon using the C I line at 9111.8 Å and oxygen using the O I triplet at 7771-7775 Å, along with the anti-correlation elements magnesium using the Mg I lines at 7691.5 and 7811.1 and aluminium using the Al I doublets at 6696-6698 Å and 7835–7836 Å. Abundances are also determined for the α-elements silicon, from two Si I lines, calcium, from five Ca I and two Ca II lines, and titanium, from the Ti II line at 6491.5 Å. The iron-peak is represented by iron, using 18 Fe I and two Fe II lines separately, and nickel, using 12 Ni I lines. Finally, abundances are also determined for potassium, using the K I resonance line at 7699 Å, and the heavy neutron-capture elements barium, using the Ba II line at 6496.9 Å, and europium, using the Eu II at 6645.1 Å.

Atomic line data were obtained from the Vienna Atomic Line Database (VALD, Piskunov et al. 1995; Kupka et al. 1999). For aluminium, we use the TOPbase oscillator strengths and new broadening data published by Nordlander & Lind (A&A, *submitted*).

As weak CN lines are present over most of the available spectral regions, the nitrogen abundance is also left as a free parameter during the abundance determination for the giant stars. We shall investigate the influence of uncertainties in the abundances of nitrogen on other species in the next section.

3.6. Abundance uncertainties

We adopt statistical uncertainties based on the χ^2 minimisation, representing photon-noise statistics. These do not take into account uncertainties in continuum placement, nor systematic modelling uncertainties. The effect of systematic errors in stellar parameters on derived chemical abundances can be estimated from the sensitivity of abundances to changes in stellar parameters. We show in Table 4 the average effect on the derived abundances from systematic changes to stellar parameters. Note however that our stars span ranges of abundances in some elements, and star-to-star variations in these sensitivities depend on e.g. the saturation level of lines.

Due to the presence of weak CN lines in most of the spectral regions, additional systematic uncertainties are present. These effects are only significant in the cooler giants. For such stars, assuming an incorrect nitrogen abundance may influence abundance determinations via line blends and depression of the continuum, and potentially indirectly via the molecular equation of state. We investigate this uncertainty by executing abundance analyses where we assume different abundances of nitrogen.

The effect of changing the assumed nitrogen abundance by 0.5 dex is roughly 0.02 dex in lithium and 0.01 dex in magnesium and titanium, while other elements are unaffected on the level of 0.01 dex. The behaviour of carbon and oxygen is somewhat involved. First, the relative abundances of carbon, nitrogen and oxygen determines the relative concentrations of different molecules in the equation of state. In particular, large

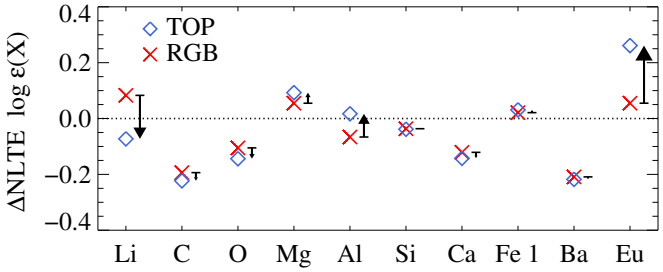

Fig. 4. NLTE effects, taken as the average difference between NLTE and LTE abundance analyses of TOP (blue diamonds) and RGB stars (red crosses). Arrows indicate the net effect on abundance differences $\Delta \log \epsilon$(TOP − RGB), with positive values represented by upward arrows. Note that europium was not possible to analyse in the TOP stars.

over-abundances of carbon may in principle lock up free atomic oxygen in the CO molecule. Furthermore, if the abundances of carbon and oxygen are derived while assuming a perturbed nitrogen abundance, then the weak CN lines will present erroneous strengths. In the RGB stars, the CN lines tend to dominate the χ^2 minimization as a function of carbon abundance, with much larger influence than the atomic carbon lines themselves. Setting the nitrogen abundance as a free parameter circumvents this problem, and allows an accurate fit of the atomic carbon lines independent of the CN line strengths. Additionally, the adopted nitrogen abundance does not seem to control the concentration of free atomic carbon and oxygen, as the influence on the strength of the atomic lines of carbon and oxygen is similar to the effects on lines of magnesium and titanium. We thus conclude that potential uncertainties in the abundance of nitrogen do not significantly affect results for other species.

3.7. NLTE and hydrodynamical effects

3.7.1. NLTE effects

We applied NLTE corrections in our line synthesis routine using precomputed grids of departure coefficients for ten elements: lithium (Lind et al. 2009b), carbon (Alexeeva & Mashonkina 2015), oxygen (Sitnova et al. 2013), magnesium (Osorio et al. 2015; Osorio & Barklem 2016), aluminium (Nordlander & Lind, A&A, *submitted*), silicon (Shi et al. 2008), calcium (Mashonkina et al. 2007), iron (Lind et al. 2012), barium (Mashonkina et al. 1999) and europium (Mashonkina & Gehren 2000). We refer the reader to each paper for details in the particular NLTE treatment, and to Piskunov & Valenti (2016) for details on the implementation of NLTE departure coefficients in SME.

For comparison, we also derived abundances using LTE line synthesis. The differences in derived abundances using NLTE line synthesis compared to the LTE case, $\Delta \log \epsilon = \log \epsilon_{\rm NLTE} - \log \epsilon_{\rm LTE}$, are on average for TOP / RGB stars, −0.07 / +0.08 dex (lithium), −0.22 / −0.19 dex (carbon), −0.14 / −0.10 dex (oxygen), +0.09 / +0.05 dex (magnesium), +0.02 / −0.07 dex (aluminium) −0.04 / −0.04 dex (silicon), −0.14 / −0.12 dex (calcium), +0.03 / +0.02 dex (neutral iron), −0.22 / −0.21 dex (barium), and +0.26 / +0.06 dex (europium). Save for lithium, aluminium, and europium, effects are similar on dwarfs and giants. The average abundance differences are illustrated in Fig. 4.

Titanium abundances were derived from Ti II, which is known to be rather unaffected by NLTE (Bergemann 2011). We have examined NLTE corrections for potassium by interpolating the grid of NLTE abundance corrections by Takeda et al. (2002).

Table 4. Abundance sensitivity to stellar parameters.

Species	$T_{\rm eff}$ + 100 K		$\log g$ + 0.1 dex		$v_{\rm mic}$ + 0.3 km s^{-1}	
	TOP	RGB	TOP	RGB	TOP	RGB
Li I	0.077	0.115	−0.001	−0.001	−0.004	0.033
C I	−0.037	−0.130	0.030	0.051	−0.013	−0.021
N (CN)	...	0.249	...	−0.021	...	−0.022
O I	−0.057	−0.092	0.030	0.034	−0.017	−0.020
Mg I	0.039	0.064	−0.004	−0.011	−0.004	−0.011
Al I	0.051	0.053	−0.003	−0.003	−0.013	−0.015
Si I	0.034	0.032	0.001	0.005	−0.002	−0.026
K I	0.072	0.111	−0.019	−0.024	−0.077	−0.148
Ca I & II	0.042	0.073	−0.002	−0.009	−0.048	−0.099
Ti II	0.043	0.060	0.036	0.025	0.007	−0.038
Fe I	0.073	0.097	−0.004	0.000	−0.036	−0.075
Fe II	0.015	−0.029	0.033	0.017	−0.012	−0.038
Ni I	0.061	0.092	0.001	0.008	−0.011	−0.070
Ba II	0.082	0.079	0.018	0.010	−0.132	−0.242
Eu II	...	0.059	...	0.044	...	−0.003

Notes. Effects on abundances are shown for the hot and cool ends of our sample, i.e. the coadded spectra RGB1 and TOP3 in Table 3.

We find corrections of −0.67 dex and −0.57 dex for stellar parameters representative of our TOP and RGB stars. Finally, we are not aware of any relevant study on NLTE effects in nickel.

3.7.2. 3D corrections

Detailed comparisons of 3D LTE and 1D LTE line formation have been performed by Dobrovolskas (2013) and Dobrovolskas et al. (2013). They compared synthetic spectra of models whose stellar parameters broadly agree with our TOP and RGB groups, and find generally vanishing 3D corrections for weak synthetic lines similar in excitation potential (but not necessarily strength) to those analysed in this work.

None of the relevant elements exhibit 3D corrections larger than 0.05 dex, and differential effects ($\Delta \log \epsilon$(TOP − RGB)) are found to be less than 0.05 dex. Their tabulations (V. Dobrovolskas, priv comm.) indicate that highly excited lines of neutral carbon and oxygen exhibit vanishingly small 3D effects at the TOP (< 0.01 dex), as well as small effects (−0.03 dex) on the RGB. However, some lines of both elements are on the verge of saturation in our spectra, and may therefore behave differently. Additionally, the excitation potential of the oxygen triplet is higher than what they investigated, which may result in a larger negative correction for weak lines in RGB models. The neutral lines of silicon exhibit identical +0.05 dex 3D corrections for the TOP and RGB models, but are again on the verge of saturation in our spectra. Magnesium and aluminium ($EW \sim 50$ mÅ) were examined only for an RGB model, indicating slight 3D corrections (+0.04 and +0.03 dex). The ionised lines of titanium ($EW < 50$ mÅ) and iron ($EW < 40$ mÅ) exhibit small positive 3D corrections in the TOP model (+0.03 dex), but essentially none in the RGB model. The neutral lines of iron and nickel, as well as the neutral and ionised lines of calcium and the ionised line of barium analysed in this work come in a wide range of strengths, most of which are unsuitably strong for these estimates. Finally, the very weak lines of the CN molecule exhibited essentially no 3D corrections.

These 3D corrections should be seen as indicative of the related uncertainties, rather than quantitative, for two reasons. First, lines analysed in this work are often saturated rather than weak. Second, hydrodynamical models differ from their 1D counterparts in typically having steeper average temperature stratification, as well as exhibiting horizontal inhomogeneities (granulation). The former will tend to exaggerate differences in line formation under LTE, as this is dictated by the temperature-sensitive Planck function. In NLTE, however, line formation depends primarily on the average radiation field, which is much more similar in the 1D and 3D cases. This point is illustrated in, e.g., Bergemann et al. (2012, see their Fig. 6).

Full 3D NLTE calculations have been performed in the analysis of very metal-poor TOP stars by Lind et al. (2013) for lithium, sodium and calcium. Their NLTE corrections for lithium and sodium are significantly larger in 3D than in the corresponding 1D cases (Lind et al. 2009a, 2011). Their NLTE corrections for calcium may be compared to the 1D case presented by Mashonkina et al. (2007), whose corrections are adopted in this work. While these two studies use different atomic models, they adopt the same inelastic hydrogen collision rates (Drawin 1968, rescaled using $S_{\rm H} = 0.1$). In both studies, the excitation and ionisation equilibria are fulfilled, indicating that NLTE corrected abundance analyses perform similarly well under 1D and 3D. The four lines in common for the two studies have NLTE corrections which are either comparable, or significantly larger in the 3D case, indicating that 3D LTE line formation may in fact be less physically realistic than 1D NLTE.

Amarsi et al. (2016) have studied the 3D NLTE line formation of oxygen in a large grid of models where $\log g \geq 3$. Their results indicate small differences between 3D NLTE and 1D NLTE for our turnoff stars, but more strongly negative 3D NLTE abundance corrections at small $\log g$. Unfortunately, their calculations cannot be applied to our RGB stars, but we may qualitatively assume that our abundances are overestimated.

Full 3D NLTE calculations have also been performed for an ultra-metal poor RGB star by Nordlander et al. (2017) for lithium, sodium, magnesium, aluminium, calcium and iron. They find similar abundances under 1D NLTE and 3D NLTE, with typically stronger NLTE effects in 3D. For these six elements they found that either, the NLTE effects are mostly negligible (lithium and sodium) with very similar results in 3D NLTE and 1D NLTE, or that they are substantial (magnesium, aluminium, calcium and iron) with significantly larger abundance

corrections in 3D NLTE by as much as 0.3 dex. Again, their results indicate that when NLTE effects are expected to be large, they are likely to dominate over the 3D effects such that 1D NLTE synthesis is preferable over 3D LTE synthesis. Additionally, it does not appear likely that NLTE effects derived from 1D models can simply be added to 3D LTE abundances, as the different temperature structures also influence the NLTE effects.

4. Results

In what follows, the derived chemical abundances are addressed for the total sample of 86 stars. The focus will predominately lie on the abundances derived from the group-averaged spectra as we consider the S/N for the warmer TOP stars too low to derive accurate per-star abundances from weak lines, as can be seen in the large scatter we find for the TOP stars compared to the RGB stars.

4.1. Abundance variations

Abundances for the group-averaged spectra were derived using the spectroscopic $T_{\rm eff}$ scale, and results are given in Table A.1 in the appendix. Generally, abundances appear to increase gradually with decreasing effective temperature. The average trends are defined as $\Delta \log \epsilon(X) = \overline{X}_{\rm TOP} - \overline{X}_{\rm RGB}$, where X is the investigated element, $\overline{X}_{\rm TOP}$ the average abundance of the three TOP groups, and $\overline{X}_{\rm RGB}$ the average abundance of the three RGB groups. The difference in stellar parameters between the two groups is about 1000 K in $T_{\rm eff}$ and 1.3 dex in $\log g$. The significance of the trend is based on the standard deviation in the two groups. The abundance trends are of the order 0.1 dex, although some elements such as carbon, oxygen, and barium seem to exhibit stronger trends (> 0.2 dex). Although the individual trends are of low significancy (1–2σ), the fact that we find consistent trends in different elements is intriguing. We will address the interpretation of these trends in Sect. 5. For now we will continue by describing the various elemental abundances.

4.2. Lithium

The line doublet at 6707.8 Å used to derived the Li abundance consist of two fine-structure components, separated by merely 0.15 Å and thus unresolved at the resolution of GIRAFFE (R = 19 000). Our atomic data takes both fine-structure and isotopic splitting into account. The abundance determination is primarily sensitive to $T_{\rm eff}$ since Li is mostly ionised in these stars. Given our $T_{\rm eff}$ precision of 100 and 50 K in dwarfs and giants, we estimate corresponding systematic abundance uncertainties of 0.08 and 0.06 dex. This dominates the systematic error budget over those due to uncertainties in gravity, metallicity and microturbulence which are only of order 0.01 dex.

We find the highest lithium abundances in the TOP stars, $T_{\rm eff} > 5900$ K, which can be identified with the field star Spite plateau. Their mean abundance A(Li) = 2.33 ± 0.10 is consistent with that derived from the coadded group-averaged spectra, 2.35 ± 0.04 as well as with the study by Mu2011, who derived a mean abundance A(Li) = 2.30 ± 0.02 (σ = 0.10). We will discuss the evolution of Li in greater depth in Sect. 5.2.

4.3. α and iron-peak elements

The analysed spectra contain lines of the α- and iron-peak elements silicon, calcium, titanium, iron and nickel. All investigated elements show weak abundance trends based on the group-averaged spectra. The sizes of the trends for Ca, Ti, Fe and Ni are summarised in Table 5. The most significant trends are found for calcium and nickel (but see discussion below), both of which are well behaved and significant on the 2σ level. The influence of errors in stellar parameters (see Table 4), given our estimated uncertainties, indicates that these systematic uncertainties cannot have spuriously created the trends.

The trends for silicon, titanium and iron are somewhat less compelling. The latter are deduced from one weak Ti II and two weak Fe II lines, meaning that they may be susceptible to the limited data quality of the spectra. As the data quality degrades towards the warmer end of the temperature range, the abundance scatter increases with it. This leads to a less precise TOP average abundance and at most marginally significant trends.The iron trend determined here is somewhat smaller than those between MS and RGB stars as found in the literature (see Table 1). Notably, our abundance trend in iron differs from the null result reported by Mu2011, who analysed the same spectra. Differences in stellar parameters are not sufficient to explain the difference, which is more likely to stem from our use of group-averaged spectra and lines of ionised species, while Mu2011 analysed lines of neutral species (in LTE) of individual stars.

We note that since the abundances of Fe and Ti are derived from lines of the ionised (majority) species, the trends are essentially immune to 3D and NLTE effects, making them rather robust (see Sects. 3.7.1–3.7.2).

Given the consistent appearance of abundance trends in five elements, in good agreement with model predictions regarding both sign and magnitude (see Sect. 5.1), we feel confident that these trends are intrinsic rather than a spurious result of uncertainties in stellar parameters and modelling errors. For example, flattening the abundance trend determined in iron would require, e.g., raising temperatures on the TOP by +450 K, or on the RGB by +250 K, in contrast to the estimated uncertainties of 100 and 50 K, respectively. Similarly, the (formally) required changes in $\log g$ or $v_{\rm mic}$ of +0.2 dex or −1.7 km s^{-1} on the TOP, or −0.4 dex or +0.6 km s^{-1} on the RGB are considered unlikely. Additionally, such changes could not *simultaneously* generate null trends in all five elements. We further investigate the sensitivity to stellar parameters in Sec. 5.3.

4.4. Light elements

4.4.1. C, N, and O

We derived carbon and oxygen abundances simultaneously from neutral atomic lines, along with nitrogen abundances from vanishingly weak CN features in the cool giants (see the discussion in Sect. 3.6). Although the individual CN lines are weak, their combined influence on the χ^2 minimisation appears sufficient to broadly classify stars as either rich or poor in nitrogen. We find the best constraints on the N abundance in our coolest RGB stars. We do not fit nitrogen abundances in the dwarfs, given the weakness (absence) of the CN features. We illustrate the variation found in these features in Fig. 5, comparing the spectra of stars with similar stellar parameters but different abundances of carbon, nitrogen and oxygen.

Carbon and oxygen abundances both exhibit a peak-to-peak scatter of 0.6 dex. Abundances derived from the group-averaged spectra show similar, strong trends with evolutionary phase: Δ(TOP − RGB) = −0.24 ± 0.10 and −0.27 ± 0.04 for C and O, respectively.

Table 5. Average abundances based on the coadded spectra and obtained at two effective temperature points.

Group	$T_{\rm eff}$ (K)	$\log g$ (cgs)	ξ (km s^{-1})	$\log \epsilon$(Mg)[a] NLTE	$\log \epsilon$(Ca)[b] NLTE	$\log \epsilon$(Ti)[c] LTE	$\log \epsilon$(Fe)[d] NLTE	$\log \epsilon$(Ni)[e] LTE
TOP	6005	4.08	1.61	6.70 ± 0.01	5.38 ± 0.03	3.98 ± 0.10	6.25 ± 0.07	4.99 ± 0.04
RGB	4927	2.80	1.33	6.75 ± 0.01	5.45 ± 0.01	4.09 ± 0.04	6.32 ± 0.02	5.07 ± 0.01
Δ(TOP − RGB)	1078	1.28	0.28	−0.05 ± 0.01	−0.07 ± 0.04	−0.11 ± 0.11	−0.07 ± 0.07	0.08 ± 0.04

Notes. The average stellar parameters for the TOP/RGB stars are averages of the three coadded spectra in each group (Table 3).

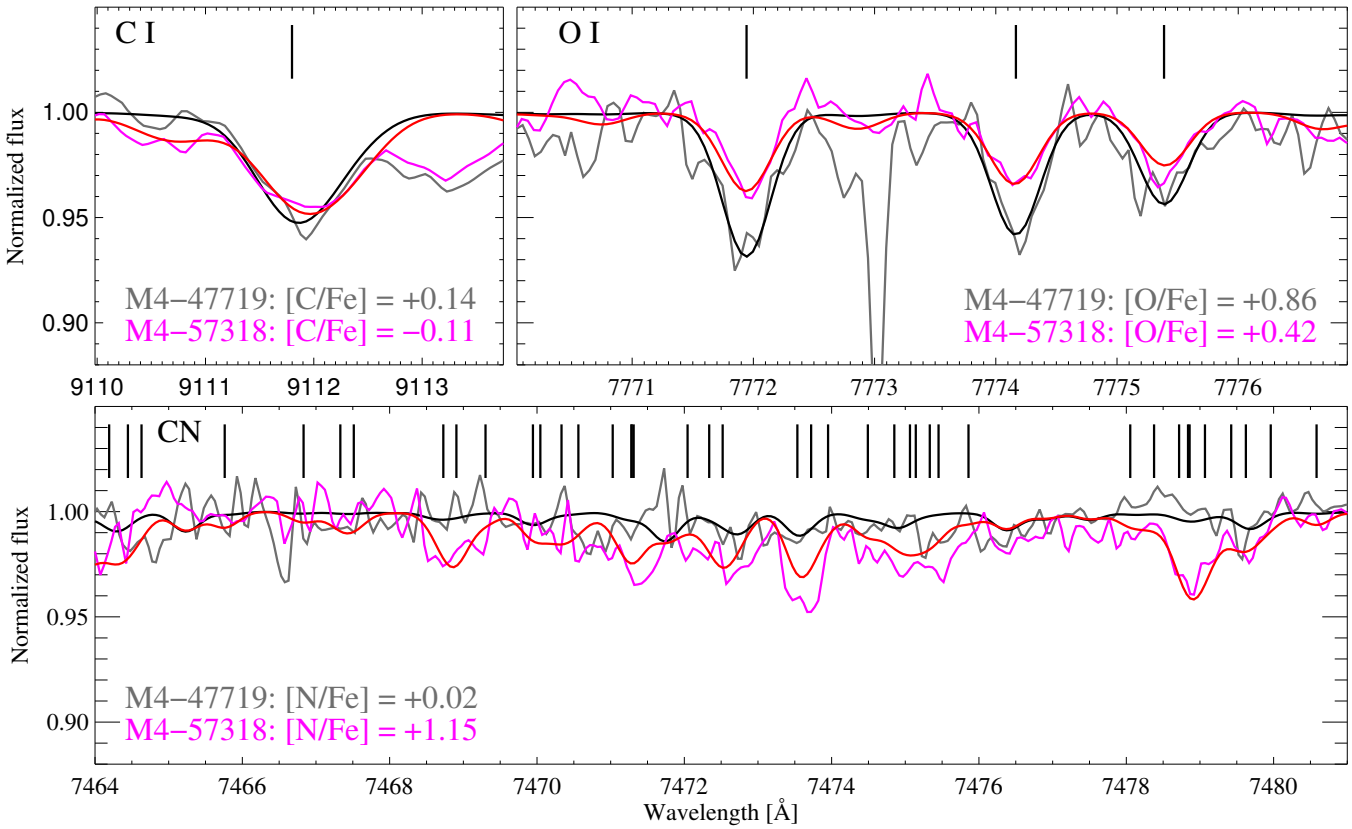

Fig. 5. Comparison of the spectra of two RGB stars with similar stellar parameters, but very different abundances of carbon, nitrogen and abundances. Features of C I, O I and the CN molecule are indicated by vertical bars in each panel. The strong spurious feature at 7773 Å in M4-47719 was automatically flagged and ignored in the analysis of the spectrum.

Comparing our C abundances, derived in NLTE from the neutral line at 9112 Å, with those derived from CN lines or the CH G-band in the blue (4200–4300Å) as found in the literature (Ivans et al. 1999; Villanova & Geisler 2011) reveals a large offset. The RGB stars studied by Ivans et al. (1999), mostly located well above the RGB bump, exhibited [C/Fe] = −0.50 (or −0.35 when adjusted to the solar abundance scale of Grevesse et al. 2007). The RGB stars studied by Villanova & Geisler (2011) on the other hand are located below the bump and exhibit somewhat higher abundances, [C/Fe] = −0.28. Our average value in the RGB stars, [C/Fe] = 0.05 ± 0.15, is significantly higher, and does not appear to change systematically over the intrinsic scatter in the most evolved giants indicating that dredge-up effects are not significant in our sample. We note that the NLTE correction for the C I line at 9112 Å in our work typically reduces the abundance by 0.2 dex. As NLTE effects are typically stronger in 3D atmospheres, it is possible that a full 3D NLTE analysis would result in an even lower abundance. However, Alexeeva & Mashonkina (2015) showed convincingly that at least for dwarfs, their NLTE analysis yields consistent abundances from atomic and molecular features. On the other hand, 3D effects on molecular features may be significant. Dobrovolskas et al. (2013) found that in RGB stars at this metallicity, 3D–1D corrections for lines of CH are of the order +0.1 dex, implying that literature values based on molecular lines are likely underestimated.

The oxygen abundances we find are again higher than those previously reported in the literature. For our RGB stars, we find a mean [O/Fe] = 0.67 ± 0.10 dex, which is similar to those of Yong et al. (2008a, [O/Fe] = 0.56, or 0.54 on our adopted abundance scale). In comparison, other values in the literature are typically lower, e.g., Marino et al. (2008, [O/Fe] = 0.39), Villanova & Geisler (2011, [O/Fe] = 0.34) and Ivans et al. (1999, [O/Fe] = 0.25). All these authors derived the O abundance from the forbidden [O I] line at 6300 Å, which is known to be rather immune to both NLTE and 3D effects, but exhibits large sensitivity to changes in $T_{\rm eff}$. For the triplet lines used in this work, 3D NLTE abundance corrections appear to be more strongly negative than the 1D NLTE corrections for giant stars, indicating that our abundances may be somewhat overestimated.

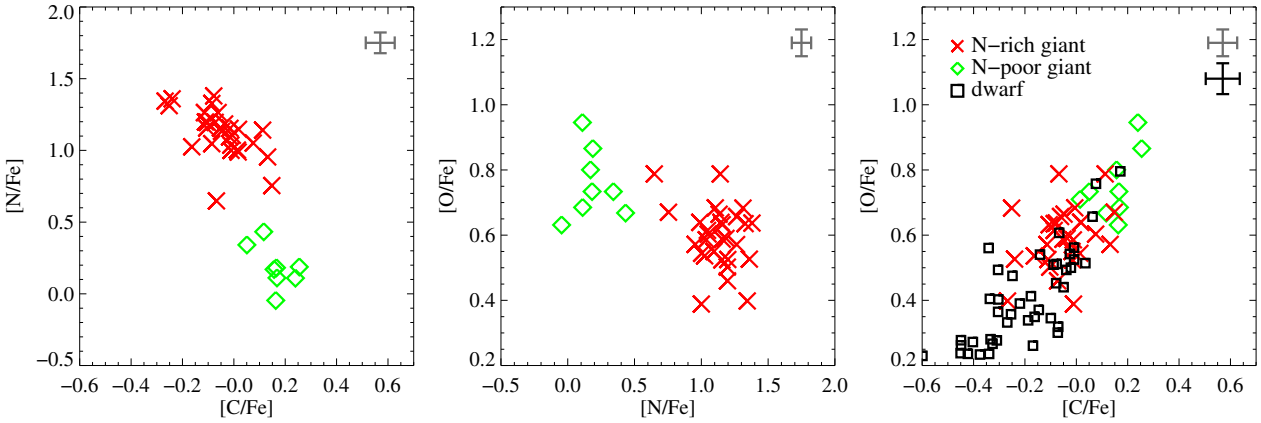

Fig. 6. Observed correlations between the light elements C, N and O. Red crosses indicate N-rich giants while N-poor giants are shown as green diamonds. We could not determine N-abundances in the dwarfs, and so compare only their abundances of C and O using black squares. Typical uncertainties on the abundances are shown in the top right corner of the panels, in gray for giants and in black for dwarfs.

Abundance ratios are compared in Fig. 6. A bimodal distribution of nitrogen abundances among the giants is apparent, with a gap near [N/Fe] ∼ 0.5. The sample thus splits into two well separated groups having different light-element contents. This behaviour was previously noted by Marino et al. (2008), and confirmed by Villanova & Geisler (2011). Both authors found also that sodium abundances correlated well with nitrogen. From their findings, they concluded that M4 has two distinct chemical populations. We confirm this conclusion and find 10 N-poor giants which belong to the first generation, and 30 N-rich giants belonging to the second generation. This indicates that about 25 % of our stars belong to the first generation. This is somewhat higher than the value found by Carretta et al. (2013, 20 %), but agrees well with the general consensus that about 1/3 of the stars in a GC belong to the first generation (see e.g. Carretta et al. 2010; Gratton et al. 2012).

Figure 6 shows the usual anti-correlations between C/O and N, where N-rich stars are characterised by low abundances of C/O, while N-poor stars exhibit high C/O abundances. In the third panel of the figure, the C-O correlation is displayed for giants and dwarfs. The relations are similar to what Marino et al. (2008) and Villanova & Geisler (2011) have found, which generally validates the N abundances we derive. We calculated the total C+N+O abundance, where possible, and find it to be constant as expected, with a mean value of 8.32 ± 0.08. This value is somewhat higher than was found by Villanova & Geisler (2011) and Ivans et al. (1999), who derived 8.16 and 8.24 respectively. Table 6 gives the average abundances for the N-poor and N-rich sub-populations. Based on this abundance data, we find that the two sub-populations identified according to [N/Fe] have significant abundance differences in their abundances of C and O, and possibly Al and Eu, but no significant differences in Li, C+N+O, Mg, Si, Ca, Ti, Fe, Ni and Ba. We will return to this in Sect. 4.4.2 and 4.5 below.

4.4.2. Mg, Al and K

Besides the light elements C, N and O, we also derive abundances for magnesium, aluminium and potassium. The Al abundances show large variations of up to 0.6 dex measured peak-to-peak. Mg and K show hardly any intrinsic variation, with peak-to-peak differences of just 0.2 dex. All elements again show evidence for a gradual increase in abundances with decreasing $T_{\rm eff}$ in the group-averaged spectra. The size of the abundance trends of Mg and K is comparable to that found for Si. Al, on the other hand, shows a stronger trend, more comparable to that of carbon or oxygen. We caution, however, that the abundances of K are likely affected by unmodelled NLTE effects.

From studies on chemical populations in globular clusters, we expect magnesium to be anti-correlated with sodium. Unfortunately we do not have information on sodium in our spectra. In massive clusters such as NGC 6752, NGC 2808 and NGC 7078, (anti-)correlations between Mg-Al and Al-Si have also been observed (Yong et al. 2005; Carretta et al. 2009a). M4, however, does not show evidence of a Mg-Al anti-correlation in our data. The (anti-)correlations between Al and O, Mg and Si for the giants are illustrated in Fig. 7 where we make a distinction between N-rich and N-poor stars, defined by a separation at [N/Fe] = 0.5. We find a clear Si-Al correlation and O-Al anti-correlation, both significant on the 3σ level (taking into account errors on both values, using the IDL routine LINMIX_ERR, see Kelly 2007) but no Mg-Al anti-correlation.

Low Al and Si abundances are only found in the N-poor stars, suggesting that a N-Al correlation is present. The average Al abundances for the two sub-populations differ by 0.13 ± 0.18 dex, where the large dispersion in the N-poor group dominates the uncertainty and thus precludes us from drawing any firm conclusion, although a correlation is formally highly significant at 4σ. We find that the stars with the lowest Al abundance are characterised by low abundances of N and correspondingly high C and O in line with the studies by Carretta et al. (2013), Marino et al. (2008) and Ivans et al. (1999). Villanova & Geisler (2011), on the other hand, did not find N-Al or Si-Al correlations and argue that a possible N-Al correlation may be spuriously caused by an unrecognised molecular line (possibly CN) blended with the Al lines at 6696–6698 Å. Our inclusion of two additional Al I lines at 7835–7836 Å should help diminish such effects. By visually inspecting the agreement of the two Al I doublets in both N-rich and N-poor stars, we conclude that the variation in Al is real, and that the N-Al and Si-Al correlation are plausible. Interesting to note are the large variations in Al and Si observed in the N-poor stars. We will come back to this in Sect. 5.4.

Table 6. Mean abundances of the two M4 sub-populations identified in the giant stars, and their combined mean values compared to literature values.

Element	N-rich	N-poor	Sun	M4	Vi2011	Mu2011[a]	Ma2011	Yo2008	Iv1999
A(Li)	1.11 ± 0.15	1.12 ± 0.15	1.05	1.11	0.97	0.92	...	...	...
[C/Fe]	−0.04 ± 0.11	0.17 ± 0.07	8.39	0.02	−0.28	...	...	...	−0.50
[N/Fe]	1.03 ± 0.16	−0.05 ± 0.34	7.78	0.76	0.48	...	...	...	0.85
[O/Fe]	0.59 ± 0.12	0.76 ± 0.11	8.66	0.64	0.34	0.30	0.39	0.56	0.25
log ϵ(C+N+O)	8.31 ± 0.07	8.36 ± 0.09	8.88	8.32	8.16	...	...	...	8.24
[Mg/Fe]	0.35 ± 0.06	0.34 ± 0.06	7.53	0.35	0.47	...	0.50	0.57	0.44
[Al/Fe]	0.51 ± 0.06	0.36 ± 0.14	6.37	0.48	0.52	...	0.54	0.74	0.64
[Si/Fe]	0.35 ± 0.06	0.33 ± 0.08	7.51	0.34	0.43	...	0.48	0.58	0.65
[K/Fe]	0.64 ± 0.09	0.69 ± 0.09	5.08	0.65	...	...	...	...	...
[Ca/Fe]	0.27 ± 0.04	0.27 ± 0.08	6.31	0.27	0.41	...	0.28	0.42	0.26
[Ti/Fe]	0.37 ± 0.08	0.33 ± 0.11	4.90	0.36	0.33	...	0.32	0.41	0.30
[Fe/H]	−1.12 ± 0.04	−1.13 ± 0.07	7.45	−1.13	−1.14	−1.11	−1.07	−1.23	−1.18
[Ni/Fe]	−0.02 ± 0.04	−0.04 ± 0.06	6.23	−0.03	−0.01	...	0.02	0.12	0.05
[Ba/Fe]	0.39 ± 0.11	0.34 ± 0.14	2.17	0.43	0.31	...	0.41	...	0.60
[Eu/Fe]	0.62 ± 0.12	0.46 ± 0.17	0.52	0.43	0.20	...	...	0.40	0.35

Notes. The fourth column gives the adopted absolute solar abundances for comparison. References are as follow: Vi2011 (Villanova & Geisler 2011), Mu2011 (Mucciarelli et al. 2011), Ma2011 (Marino et al. 2008), Yo2008 (Yong et al. 2008a,b), and Iv1999 (Ivans et al. 1999). [(a)] These [O/Fe] values refer to abundances from Lovisi et al. (2010). We quote the combined median value for SGB and RGB stars, as given by Mucciarelli et al. (2011).

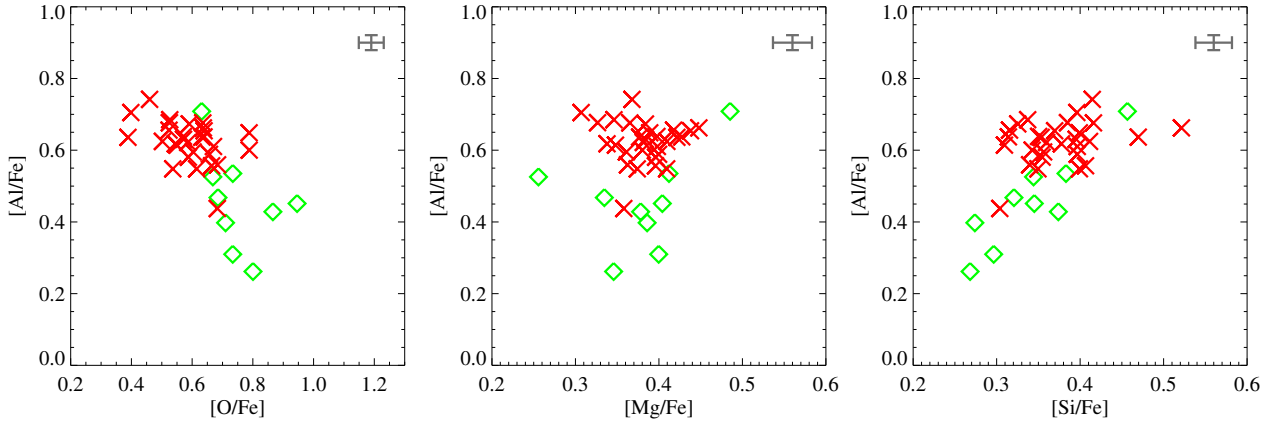

Fig. 7. Observed correlations between aluminium and the light elements O, Mg and Si in giant stars. The symbols and colours are the same as in Fig. 6. The black cross in the top right corner of each panel represents the typical error on the abundances.

4.5. Heavy elements

We derived abundances for barium and europium. These neutron-capture elements give us information about nucleosynthesis processes which occurred in the cluster. Barium is a pure s-process element, while europium is primarily an r-process element. Our NLTE Ba abundances yield averages of [Ba/Fe] = 0.43 ± 0.07 and 0.27 ± 0.08 for the group-averaged RGB and TOP stars, respectively. Comparison values for RGB stars in the literature are 0.60 ± 0.10, 0.41 ± 0.09, 0.50 ± 0.12 and 0.32 ± 0.04 from Ivans et al. (1999), Marino et al. (2008), D'Orazi et al. (2010) and Villanova & Geisler (2011), respectively.

Europium abundances were primarily derived for the RGB stars as the weak 6645.1 Å Eu II line disappears in the noise for the warmer stars in the sample. In total we derived reliable NLTE abundances for 38 RGB stars ($T_{\rm eff}$< 5200 K), with a dispersion of 0.10 dex. The group-averaged spectra indicate [Eu/Fe] = 0.43 ± 0.10, which is compatible with the literature: 0.35 (Ivans et al. 1999), 0.40 (Yong et al. 2008b) and 0.20 (Villanova & Geisler 2011). Abundances derived from individual spectra are significantly higher than those based on the group-averaged coadded spectra, due to the weakness of the spectral line.

Our resulting [Ba/Eu] ratio based on RGB group-averaged spectra is 0.00 ± 0.12, while Ivans et al. (1999) find +0.25, and +0.11 was reported by Villanova & Geisler (2011). In a differential study between M4 and M5, Yong et al. (2008a) found that the stars in M4 were formed from gas that was enriched in s-process products but deficient in r-process products relative to M5. Combining their [Eu/Fe] ratios with [Ba/Fe] values from Ivans et al. (1999), an average [Ba/Eu] = 0.19 value is found. Our result instead implies that stars in M4 have a very similar s-to-r contribution than the Sun, and that previous results should rather be interpreted as other clusters being poor in s-process or rich in r-process elements. Based on the value Ivans et al. (1999) found, they suggested that the period of star formation and mass loss that preceded the formation of the second generation stars in M4 was long enough for AGB stars to pollute the primordial

interstellar matter in the cluster by their ejecta. Part of the disagreement with results in the literature are due to our application of NLTE corrections, which have significant magnitude and opposite sign for Ba (−0.20) and Eu (+0.08), resulting in a net correction on [Ba/Eu] of −0.28 dex. This behaviour is qualitatively expected from previous studies in the literature using the same NLTE model, albeit on more metal-poor stars (Mashonkina & Christlieb 2014).

5. Discussion

5.1. Atomic diffusion trends

Abundance trends with $T_{\rm eff}$ for magnesium, calcium, titanium and iron are shown in Fig. 8. The squares in the figure represent the abundances derived from the coadded group-averaged spectra, while abundances for the individual stars are shown as grey diamonds. The overplotted solid lines are predictions from stellar evolution models computed at the cluster's metallicity [Fe/H] = −1.1 and age of 12 Gyr. The dashed lines indicate the initial abundances of the models. The models include the effects of atomic diffusion (AD) and additional mixing (AddMix). The effects of AD are modelled from first principles while the AddMix is a mixing process added to the models in an ad-hoc fashion as a diffusive process with no assumption on its physical origin. AddMix is given as a function of temperature and density (i.e., depth), with a parametrised efficiency. The exact formalism of AddMix can be found in Richard et al. (2005).

The abundance trends in Fig. 8 are compared to AD models at three different efficiencies of AddMix. The T6.0 ($\log T_0$ = 6.0) grid of models represents models with low efficiency of AddMix, which has previously been found to well match observations in NGC 6397 (Korn et al. 2007; Lind et al. 2008; Nordlander et al. 2012). The T6.2 ($\log T_0$ = 6.2) models have a higher efficiency of AddMix, meaning that the effects of AD on the surface abundances are even more reduced, thus resulting in weaker abundance trends as compared to the T6.0 models. This grid of models with higher efficiency was preferred to explain the trends observed in NGC 6752 (Gruyters et al. 2013, 2014). With our current results, we again clearly prefer the T6.2 models over T6.0. We have also included models with even higher efficiency of AddMix (T6.3, $\log T_0$ = 6.3) to see if the efficiency can be better constrained. The observed scatter in the abundances determined from the warm dwarf stars, however, does not allow us to give a definite answer. The effects on surface abundances in turnoff stars differ between the T6.2 and T6.3 models by just 0.02 dex for elements like carbon, oxygen, magnesium and silicon, but even less for calcium, titanium and iron-peak elements. Effects on lithium however differ by 0.4 dex, due to the large amount of burning caused by deeper mixing in the T6.3 grid of models. We thus prefer the T6.2 models over T6.3 on the grounds of remaining conservative in estimating the effects on lithium (see Sect. 5.2).

5.2. Evolution of lithium

We compare lithium abundances to model predictions in Fig. 9. While the models of low-efficiency AddMix, T6.0, predicts a slight upturn in surface lithium abundances as stars evolve onto the SGB, the higher-efficiency model T6.2 predicts instead a slight decrease. This is a direct consequence of the depth down to which AddMix operates. In the low-efficiency models, the Li abundance increases with depth below the convective zone during the main sequence due to atomic diffusion, in layers where the temperature is not high enough to have nuclear destruction of Li. When the star evolves of the main sequence, the convection zone expands inwards and the settled material resurfaces.

By contrast, in the higher-efficiency T6.2 models AddMix operates over a deeper extent in the star and atomic diffusion is sufficiently reduced to avoid the formation of a Li gradient (see section 3.4.3 of Richard et al. 2005 for more details). As the convection zone expands inward, lithium-depleted material dilutes the surface composition. In the model with highest efficiency of AddMix, lithium is brought directly to regions where temperatures are sufficient for nuclear burning, resulting in strongly depleted surface layers.

This same dilution mechanism is responsible for the rapid decrease in surface lithium abundances along the SGB, during the first dredge-up. Firstly, we find that abundances at the TOP-SGB transition, A(Li) = 2.30 ± 0.16, are (insignificantly) lower than those on the TOP, A(Li) = 2.32 ± 0.10, which disfavours the lithium turn-up predicted by the low-efficiency AddMix model. Secondly, we find that the observed smooth decrease in lithium abundances during the first dredge-up match predictions well. Following the dredge-up, a plateau is reached on the RGB, with an average abundance of A(Li) = 1.06 ± 0.09, consistent with that of the coadded group-averaged spectra of the first two RGB groups, which both indicate A(Li) = 1.06. Finally, lithium abundances drop abruptly on the cool end of the RGB, with three stars exhibiting values significantly below the plateau, averaging A(Li) = 0.44 ± 0.07. The physics of this extra-mixing episode, likely caused by thermohaline mixing, are not included in our models, but are available and well described elsewhere (e.g., Charbonnel & Lagarde 2010).

The evolution of Li is qualitatively consistent with that presented by Mu2011. Comparing our lithium abundances, we find a fully consistent result among the TOP stars, while our abundances are higher on the RGB plateau by 0.14 dex and after the extra-mixing episode by 0.21 dex. The rather large difference for RGB stars cannot be explained by differences in stellar parameters (our $T_{\rm eff}$ values are lower by 58 ± 21 K, leading to *lower* abundances by 0.07 dex) and NLTE corrections (their corrections are *higher* by roughly 0.10 and 0.15–0.20 dex at the lower and upper stages on the RGB).

We correct the observed lithium abundances for the predicted amount of depletion using the T6.2 models, resulting in an average initial lithium abundance of $A(\mathrm{Li})_{\rm init}$ = 2.59 ± 0.10 among the TOP stars. This is in excellent agreement with the corresponding value recovered from the RGB plateau, 2.56 ± 0.09, or the full sample of stars (excluding the three brightest RGB), 2.57 ± 0.10. We adopt the value measured from the TOP stars as our recommended value, and note its very close agreement with values determined for NGC 6752 (2.58 ± 0.10 or 2.53 ± 0.10, Gruyters et al. 2013, 2014), NGC 6397 (2.57 ± 0.10, Nordlander et al. 2012) and M30 (2.48 ± 0.10, Gruyters et al. 2016).

Unfortunately, physical shortcomings of the stellar evolution models aside, considerable uncertainty stems from the selection of the AddMix efficiency. For example, selecting a weaker efficiency T6.0 results in an average initial abundance of 2.53, while the more efficient T6.25 and T6.3 indicate average initial lithium abundances of 2.72 and 2.99, albeit with considerably larger differences between the initial abundances deduced from TOP and RGB stars of 0.09 and 0.19 dex, respectively. As noted in the previous section, the evolutionary effects of AddMix efficiencies in the range T6.2–T6.3 on elements other than lithium are treacherously indistinguishable. This makes an accurate inference of the initial lithium abundance on RGB stars alone, as proposed by Mucciarelli et al. (2012), very difficult (see also Korn 2012).

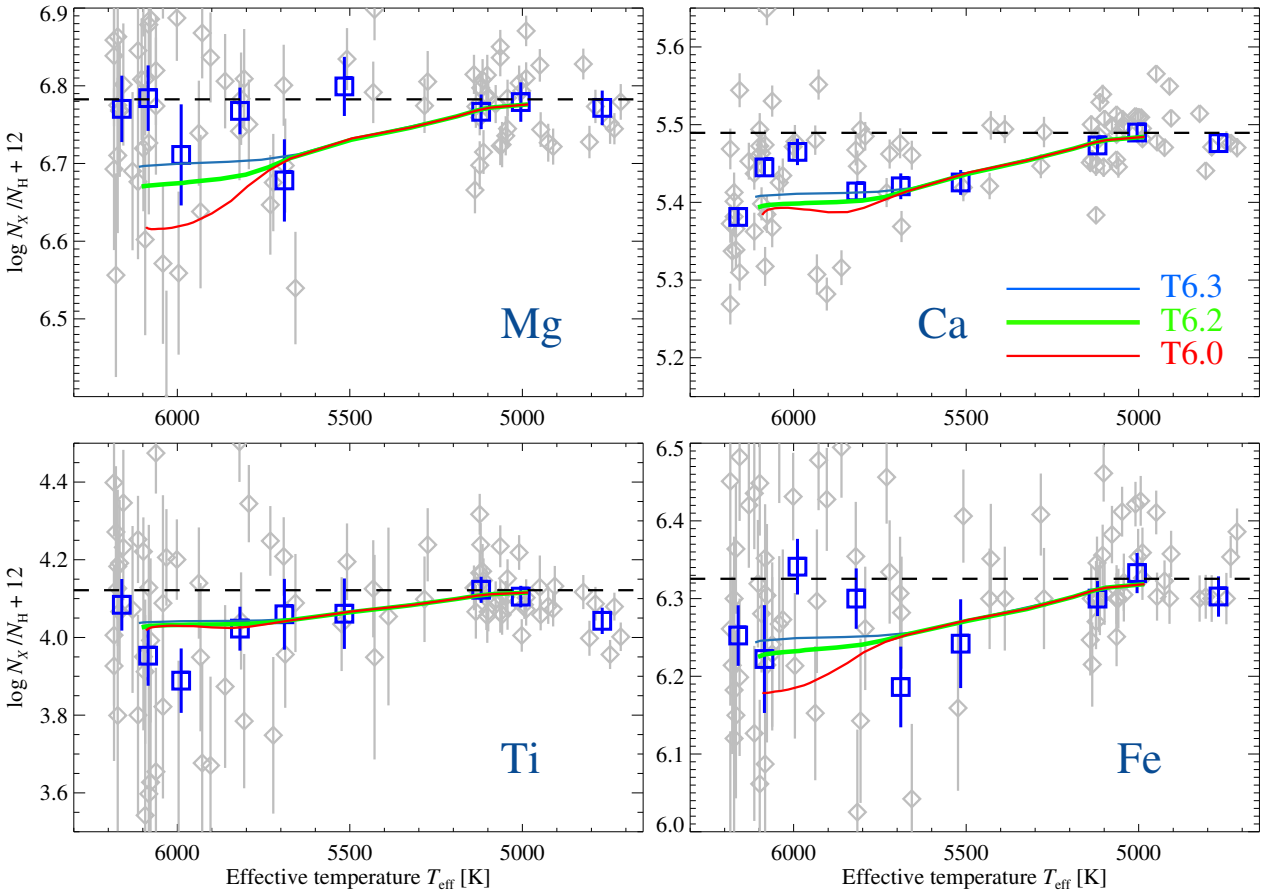

Fig. 8. Evolutionary abundance trends of Mg, Ca, Ti and Fe. Mg abundances are derived from neutral lines, while Ti and Fe are derived from lines of singly ionised species, and Ca is based on a mixture of lines of both neutral and singly ionised species. The trends are compared to predictions from stellar structure models including atomic diffusion with additional mixing with different efficiencies, at an age of 12 Gyr. Horizontal, dashed lines represent the initial abundances of the models, which have been adjusted so that predictions match the observed abundance level of the coolest stars. Blue squares represent results for group-averaged coadded spectra, while gray diamonds represent results for individual stars.

Finally, we have not accounted for Galactic production of lithium when deriving the initial Li abundance content of the cluster. The empirical trends of Li abundance with metallicity are found to vary in the literature. Ryan et al. (1999) and Asplund et al. (2006) find trends as steep as 0.1 dex per 1 dex in [Fe/H] while Meléndez & Ramírez (2004) and Shi et al. (2007) find no trend at all. The different findings are largely the result of differences in the adopted $T_{\rm eff}$ scales. On the theoretical side, Prantzos (2012) predicts a (Galactic) production of merely 0.05 dex at this metallicity, due mainly to ν-nucleosynthesis in core-collapse supernovae rather than spallation by cosmic rays. Accounting for post-primordial production by applying, e.g., an 0.1 dex downward correction of the derived stellar lithium abundance weakens the agreement with the CMB-calibrated BBN primordial Li value. However, as stated above, a gap of 0.1–0.2 dex can be explained by adopting a slightly more efficient AddMix.

Another possibility was suggested by Piau et al. (2006). They argue that part of the discrepancy (of order 0.2 to 0.3 dex) between the observed Li plateau and the BBN-predicted primordial Li abundance is explained by Population III stars that efficiently depleted lithium. This scenario was, however, criticised by Prantzos (2006) who argued that even a slight depletion of lithium would likely be accompanied by prohibitively large oxygen production in these stars. Furthermore, one would expect the amount of mixing through Population III stars to vary depending on the mass of the Galaxy. Instead, lithium abundances in the Sagittarius globular cluster M54, and in the remnant dwarf galaxy ω Centauri, are similar to those found in Galactic field stars (Monaco et al. 2010; Mucciarelli et al. 2014).

5.3. The $T_{\rm eff}$ scale

The magnitude of the abundance trends is a topic of debate and as shown by the discussion in Sect. 3.4.2 susceptible to errors in $T_{\rm eff}$. To check whether the trends are spurious results of potential biases in the temperature scale, we executed the analysis on two other temperature scales. We refer to our main temperature scale, derived from the $(V-I)$–$T_{\rm eff}$ relations of Ramírez & Meléndez (2005), as $T_{\rm eff,\,phot}$, the spectroscopic $T_{\rm eff}$ scale constructed to uphold the ionisation equilibrium between Fe I and Fe II as $T_{\rm eff,\,ion}$, and the spectroscopic $T_{\rm eff}$ scale constructed to produce a flat abundance trend deduced from Fe I as $T_{\rm eff,\,flat}$.

The spectroscopic and photometric $T_{\rm eff}$ scales are affected by different types of biases. For example, the photometric $T_{\rm eff}$ scale obtained via calibration of observed photometric colours on the infrared flux method (IRFM) is largely insensitive to uncertainties in model atmospheres (e.g., the adopted line broadening recipe, or the assumption of LTE and 1D geometry). It can, however, be affected by uncertainties in the raw photome-

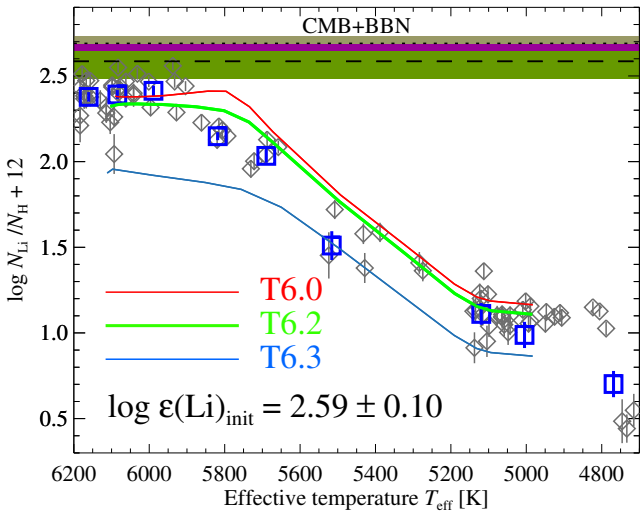

Fig. 9. Observed lithium abundances, compared to stellar evolution model predictions for different efficiencies of AddMix (see text). Measurements for individual stars are shown as grey diamonds, while squares correspond to the Li abundances derived from coadded spectra. The initial, i.e., diffusion-corrected, abundance of the models, log ϵ(Li) = 2.59 ± 0.10, shown by the horizontal dashed line and shaded region, compares well to the predicted primordial lithium abundance, log ϵ(Li) = 2.67 ± 0.07, shown by the dotted horizontal line and shaded region.

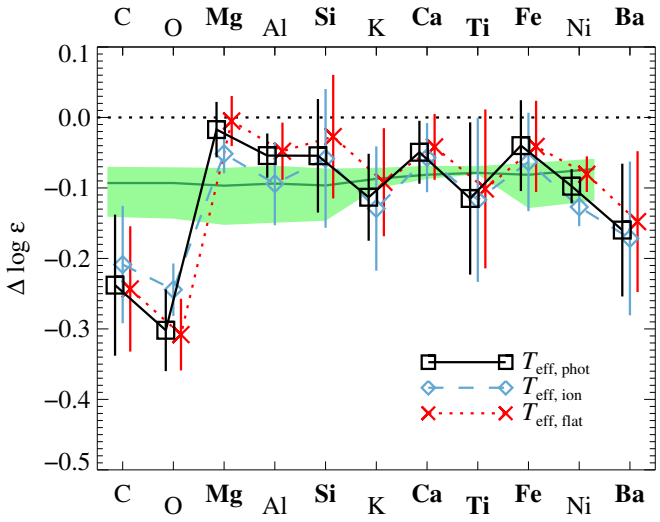

Fig. 10. Elemental abundance trends on three different $T_{\rm eff}$ scales determined from group-averaged coadded spectra, connected by lines for clarity, with vertical lines indicating the standard deviation. The abundance of iron is based on Fe II lines. The shaded background indicates the range of model predictions for different efficiencies of AddMix, with the T6.2 model indicated by a line.

try, non-linearities and jumps in the response of $T_{\rm eff}$ to photometric colour or chemical composition, lacking or uneven coverage in parameter space, uncertainties in reddening, etc. The spectroscopic $T_{\rm eff}$ scales are directly sensitive to uncertainties in the model atmospheres and in line formation, as well as the quality of the spectra.

Results of the three abundance analyses are compared in Fig. 10, where we also compare to model predictions. Abundance trends on the different temperature scales do not vary significantly, and the trends in carbon, oxygen, aluminium, potassium, calcium, titaium, nickel, and barium remain formally statistically significant with at least 1σ on all three $T_{\rm eff}$ scales. This, in line with the reasoning in Sect. 3.6, verifies that the observed abundance trends are indeed robust to uncertainties in the stellar parameters.

5.4. The formation of M4

M4 is characterised by a bimodal N distribution and bimodal Na-O anti-correlation (Villanova & Geisler 2011), a C-O correlation and N-O anti-correlation (Ivans et al. 1999), and the lack of an Mg-Al anti-correlation (Villanova & Geisler 2011, this work). Given the bimodal N distribution, the simplest explanation for these abundance patterns is a self-pollution scenario in which a first generation of stars, formed out of primordial, O-rich, Na-poor material, pollutes the interstellar medium by nucleosynthesis products which are depleted in O and enriched in Na. After some 100 million years, a new epoch of star formation is triggered by the onset of supernovae and a second generation of stars is formed out of the polluted medium. The deep potential well of the most massive globular clusters could even retain and mix interstellar gas with the expelled material from the second generation and trigger a third star-formation epoch.

The origin of the pollution is debated. Possible candidates include massive MS stars, either fast-rotating or binaries, and intermediate-mass AGB stars. The observed (anti-)correlations then characterise stars from previous generations and hold the key to identify the pollution mechanism(s). As M4 does not show evidence of a Mg-Al anti-correlation, one would assume that the Mg-Al burning cycle did not activate in the polluters. This then implies that the stars responsible for the pollution of the second generation did not reach core temperatures higher than about 50×10^6 K, the onset temperature of the Mg-Al burning cycle (Decressin et al. 2007). If we assume that the polluters were fast-rotating massive stars (FRMS), we can use the models by Decressin et al. (2007) together with the derived [Mg/Al] and [C/N] ratios to deduce an upper limit to the mass of the polluters. Based on the range of the observed [Mg/Al] ratios ($-0.24 <$ [Mg/Al] < 0.40), which are mainly due to variations in Al, together with Fig. 12 of Decressin et al. (2007), we find an upper-mass limit between 20 and 40 $M_\odot$. This is consistent with the upper-mass limit given by Villanova & Geisler (2011) based on the range in the [O/Na] ratio they observed and Fig. 10 in Decressin et al. (2007). However, when comparing the model predictions to the observed range in [C/N] ratios ($-1.53 <$ [C/N] < 0.41), the models fail as they cannot account for the observed high end of the distribution. If we disregard the N-poor stars, where abundances are most uncertain, the range ($-1.52 <$ [C/N] < -0.53) is in line with the predicted range of the 40 $M_\odot$ model. These abundance-ratio variations together with the observed N-Al and Si-Al correlations seem to suggest the Mg-Al cycle was active, as the Si-Al correlation is a direct result of leakage from the Mg-Al cycle on ^{28}Si, which requires temperatures of at least 65×10^6 K (Carretta et al. 2009a). Evidence for an active Mg-Al cycle was also presented by Marino et al. (2011). This suggests that the pollution scenario involves pollution by FRMS of the order of 40 $M_\odot$. However, the high [C/N] values detected in the N-poor stars may suggest the presence of other pollution mechanisms.

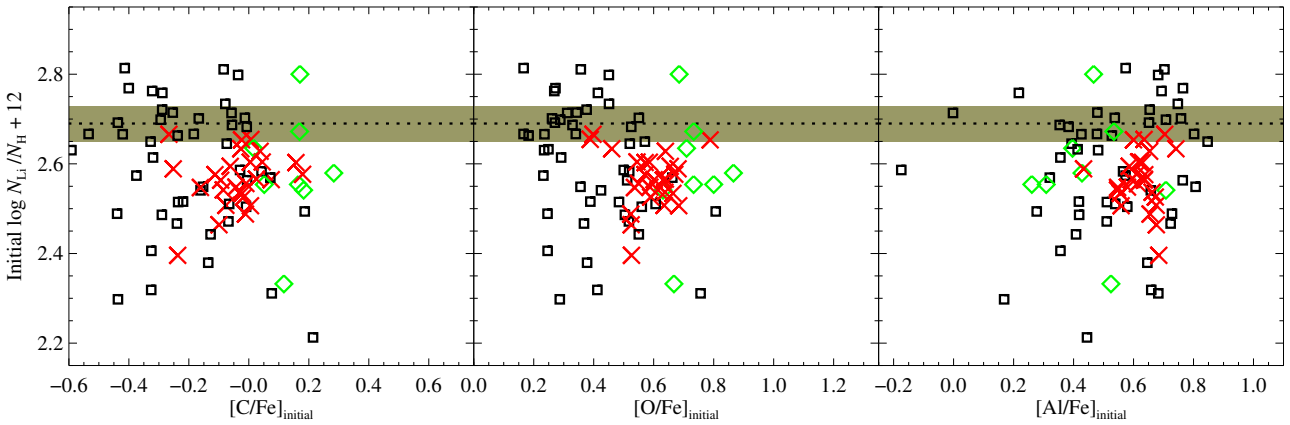

Fig. 11. Abundances of lithium compared to the abundance ratios over iron of carbon (left), oxygen (middle) and aluminium (right). All abundances have been corrected for the evolutionary effects of atomic diffusion and dredge-up. The predicted primordial lithium abundance based on CMB-calibrated BBN calculations (see text) is indicated by the dotted line and shaded region. Symbols and colours are the same as in Fig. 6, with small black squares representing dwarfs, and red crosses and green diamonds representing N-poor and N-rich giants, respectively.

Villanova & Geisler (2011) ruled out a pollution scenario in which the second generation of stars was born from material polluted by AGB stars. They found that the barium abundances they derived for a group of RGB stars in M4 do not show a bimodal behaviour, while the yttrium abundances do. They then argue that since their observations are not in line with recent AGB yields calculated by Karakas et al. (2010) which indicate a similar behaviour for the s-process elements if the pollution is driven by massive AGB stars, the AGB scenario is not plausible. Recently D'Orazi et al. (2013) reinvestigated the possibility that the pollution might be caused by AGB stars and argues that AGB stars can not be ruled out as contributors to the pollution. We can check for a possible contribution of AGB-star pollution by noting that AGB stars can produce Li through the Cameron-Fowler mechanism (Cameron & Fowler 1971). Fig. 11 compares the initial abundances of lithium, carbon, oxygen and aluminium after correcting for the evolutionary effects of AD and dredge-up. In the panels, the black squares give the abundances derived from the spectra of dwarfs, the green diamonds and red crosses give the abundances for N-poor and N-rich giants, respectively. There are no clear correlations visible in the [C/Fe]-A(Li) or [O/Fe]-A(Li) planes. As the sample consists of a random mixture of first and second generation stars, the lack of such correlations can be seen as evidence for Li production as was suggested by Mu2011. The Cameron-Fowler mechanism is, however, susceptible to the assumed mass-loss rates and quite some fine-tuning is needed to achieve the uniform Li abundances in M4.

In light of the findings here as well as in the literature, we suggest a scenario in which the pollution is caused by both FRMS and AGB stars. We envision that the most massive stars ($\sim 40\,M_\odot$) of the first generation are FRMS which are responsible for the initial pollution, followed by a second injection of polluted material when the intermediate-mass stars ($\sim 10\,M_\odot$) reached the AGB phase. Highly precise s-process abundance determinations for first- and second-generation stars with well-characterised light element abundances could be used to verify or rule out this scenario.

Finally, we note that our NLTE abundance analysis results in a ratio [Ba/Eu] = 0.00 ± 0.12, or $\log\varepsilon$(Ba/Eu) = 1.62 on the absolute scale. This is rather low compared to literature values, and would seem to indicate a solar s-process contribution in a cluster which is typically regarded as strongly s-process enhanced. We emphasise that our abundance results should be compared to other NLTE studies, e.g. the results of Mashonkina & Gehren (2001, their Fig 8), where field dwarfs exhibit [Ba/Eu] ≈ −0.5 at this metallicity. Our abundance ratio is significantly higher (by a factor 7) than the pure r-process ratio $\log\varepsilon$(Ba/Eu) = 0.77 derived empirically by Mashonkina & Christlieb (2014), using the same NLTE model as in this and the aforementioned work. In light of the rather large magnitude of NLTE corrections on the abundance ratio in this case, and the dependence of these corrections on stellar parameters and the elemental abundances, we urge the community to take NLTE corrections into account in future work.

6. Summary

Our chemical abundance analysis indicates the existence of weak abundance trends along the subgiant branch in magnesium, silicon, calcium, titanium and iron. We find that these trends are robust to modelling uncertainties, as well as uncertainties in the $T_{\rm eff}$ scale. The observed trend in iron would, e.g., require changes of several hundred kelvin to flatten completely. Additionally, the trends are found to be in very good agreement with predictions from stellar structure models including atomic diffusion (AD) moderated by efficient additional mixing (AddMix). We also find statistically significant trends in carbon, oxygen, aluminium, potassium, nickel and barium, which are robust to uncertainties in the $T_{\rm eff}$ scale. We caution that some of these trends, such as the Al and K trends, may be significantly distorted by differential NLTE effects.

In the current formulation of the AddMix mechanism, its efficiency needs to be at least T6.2 in order to reproduce the observed trends, which is in agreement with results from NGC 6752 ([Fe/H] = −1.6, Gruyters et al. 2013, 2014). This is in contrast to the very metal-poor clusters NGC 6397 ([Fe/H] = −2.1, Korn et al. 2007; Lind et al. 2008; Nordlander et al. 2012) and M30 ([Fe/H] = −2.3, Gruyters et al. 2016) where weak efficiencies of AddMix, T6.0 and T5.8, respectively, are required to match observations. After correcting our measured lithium abundances for the predicted effects of AD, we determine an average initial lithium abundance of $A(\mathrm{Li})_{\rm init}$ = 2.59 ± 0.10 for

TOP stars in M4. We note that results from the four globular clusters indicate consistent diffusion-corrected initial lithium abundances, in the very narrow range $A(\mathrm{Li})_{\mathrm{init}} = 2.48$ (Gruyters et al. 2016) to 2.59 (this work), fully compatible with each other within the associated errors.

In order to constrain the properties of first-generation polluters in the cluster, we have compared abundances of elements that form under different conditions. The observed range of the abundance ratio [Mg/Al] is consistent with an upper mass limit for the polluting stars of 20–40 $M_{\odot}$ (Decressin et al. 2007), in agreement with what Villanova & Geisler (2011) deduced from the same theoretical models using the corresponding range in [O/Na]. We cannot, however, reconcile our non-detection of a Mg-Al anti-correlation with the detected N-Al and Si-Al correlations which indicate leakage from an active Mg-Al cycle. We thus ask stellar modellers to further investigate possible evolutionary scenarios which could generate these abundance patterns.

Acknowledgements. The authors wish to thank Yeisson Osorio, Lyudmila Mashonkina, Tatyana Sitnova and Sofia Alexeeva for performing NLTE calculations specifically for this work. We also wish to thank Yassan Momany for providing the photometric catalogue of M4, and Vidas Dobrovolskas for providing us with tabulations of his 3D abundance corrections. PG and AK thank the European Science Foundation for support in the framework of EuroGENESIS. TN and AK acknowledge support by the Swedish National Space Board. O.R. acknowledges HPC@LR and Calcul Québec for providing the computational resources required for the stellar evolutionary computations. O.R. also acknowledges the financial support of Programme National de Physique Stellaire (PNPS) of CNRS/INSU.

References

Alexeeva, S. A. & Mashonkina, L. I. 2015, Monthly Notices of the Royal Astronomical Society, 453, 1619
Alonso, A., Arribas, S., & Martínez-Roger, C. 1999, A&AS, 140, 261
Alonso, A., Arribas, S., & Martínez-Roger, C. 2001, A&A, 376, 1039
Amarsi, A. M., Asplund, M., Collet, R., & Leenaarts, J. 2016, Monthly Notices of the Royal Astronomical Society, 455, 3735
Anders, M., Trezzi, D., Menegazzo, R., et al. 2014, Physical Review Letters, 113, 042501
Asplund, M., Lambert, D. L., Nissen, P. E., Primas, F., & Smith, V. V. 2006, ApJ, 644, 229
Barklem, P. S., Stempels, H. C., Allende Prieto, C., et al. 2002, Astronomy and Astrophysics, 385, 951
Bergemann, M. 2011, MNRAS, 413, 2184
Bergemann, M., Lind, K., Collet, R., Magic, Z., & Asplund, M. 2012, MNRAS, 427, 27
Blackwell, D. E., Booth, A. J., Petford, A. D., et al. 1986, MNRAS, 221, 427
Cameron, A. G. W. & Fowler, W. A. 1971, ApJ, 164, 111
Carretta, E., Bragaglia, A., Gratton, R., & Lucatello, S. 2009a, A&A, 505, 139
Carretta, E., Bragaglia, A., Gratton, R. G., et al. 2009b, A&A, 505, 117
Carretta, E., Bragaglia, A., Gratton, R. G., et al. 2010, A&A, 516, A55
Carretta, E., Gratton, R. G., Bragaglia, A., D'Orazi, V., & Lucatello, S. 2013, A&A, 550, A34
Charbonnel, C. & Lagarde, N. 2010, A&A, 522, A10
Coc, A., Uzan, J.-P., & Vangioni, E. 2013, arXiv:1307.6955
Cudworth, K. M. & Rees, R. 1990, AJ, 99, 1491
Cyburt, R. H., Fields, B. D., Olive, K. A., & Yeh, T.-H. 2016, Reviews of Modern Physics, 88, 015004
Decressin, T., Meynet, G., Charbonnel, C., Prantzos, N., & Ekström, S. 2007, A&A, 464, 1029
Dobrovolskas, V. 2013, PhD Thesis
Dobrovolskas, V., Kučinskas, A., Steffen, M., et al. 2013, A&A, 559, A102
D'Orazi, V., Campbell, S. W., Lugaro, M., et al. 2013, MNRAS, 433, 366
D'Orazi, V., Gratton, R., Lucatello, S., et al. 2010, ApJ, 719, L213
Drake, J. J., Smith, V. V., & Suntzeff, N. B. 1994, ApJ, 430, 610
Drawin, H.-W. 1968, Zeitschrift fur Physik, 211, 404
Ferraro, F. R., Sabbi, E., Gratton, R., et al. 2006, ApJ, 647, L53
Gratton, R. G., Carretta, E., & Bragaglia, A. 2012, A&A Review, 20, 50
Grevesse, N., Asplund, M., & Sauval, A. J. 2007, Space Sci. Rev., 130, 105
Gruyters, P., Korn, A. J., Richard, O., et al. 2013, A&A, 555, A31
Gruyters, P., Lind, K., Richard, O., et al. 2016, Astronomy & Astrophysics, 589, A61
Gruyters, P., Nordlander, T., & Korn, A. J. 2014, A&A, 567, A72
Gustafsson, B., Edvardsson, B., Eriksson, K., et al. 2008, A&A, 486, 951
Hendricks, B., Stetson, P. B., VandenBerg, D. A., & Dall'Ora, M. 2012, AJ, 144, 25
Ivans, I. I., Sneden, C., Kraft, R. P., et al. 1999, AJ, 118, 1273
Karakas, A. I., Campbell, S. W., Lugaro, M., Yong, D., & Chieffi, A. 2010, Mem. Soc. Astron. Italiana, 81, 1010
Kelly, B. C. 2007, ApJ, 665, 1489
Korn, A. J. 2012, Memorie della Societa Astronomica Italiana Supplementi, 22, 64
Korn, A. J., Grundahl, F., Richard, O., et al. 2007, ApJ, 671, 402
Kupka, F., Piskunov, N., Ryabchikova, T. A., Stempels, H. C., & Weiss, W. W. 1999, A&AS, 138, 119
Lardo, C., Salaris, M., Savino, A., et al. 2016, arXiv:1612.08929 [astro-ph]
Lind, K., Asplund, M., & Barklem, P. S. 2009a, A&A, 503, 541
Lind, K., Asplund, M., Barklem, P. S., & Belyaev, A. K. 2011, A&A, 528, A103
Lind, K., Bergemann, M., & Asplund, M. 2012, MNRAS, 427, 50
Lind, K., Korn, A. J., Barklem, P. S., & Grundahl, F. 2008, A&A, 490, 777
Lind, K., Melendez, J., Asplund, M., Collet, R., & Magic, Z. 2013, A&A, 554, A96
Lind, K., Primas, F., Charbonnel, C., Grundahl, F., & Asplund, M. 2009b, A&A, 503, 545
Lovisi, L., Mucciarelli, A., Ferraro, F. R., et al. 2010, ApJ, 719, L121
Ludwig, H.-G., Behara, N. T., Steffen, M., & Bonifacio, P. 2009, Astronomy and Astrophysics, 502, L1
MacLean, B. T., Campbell, S. W., De Silva, G. M., et al. 2016, Monthly Notices of the Royal Astronomical Society: Letters, slw073
Malavolta, L., Sneden, C., Piotto, G., et al. 2014, AJ, 147, 25
Marino, A. F., Villanova, S., Milone, A. P., et al. 2011, ApJ, 730, L16
Marino, A. F., Villanova, S., Piotto, G., et al. 2008, A&A, 490, 625
Marquardt, D. W. 1963, SIAM J. Appl. Math., 11, 431
Mashonkina, L. & Christlieb, N. 2014, A&A, 565, A123
Mashonkina, L. & Gehren, T. 2000, A&A, 364, 249
Mashonkina, L. & Gehren, T. 2001, A&A, 376, 232
Mashonkina, L., Gehren, T., & Bikmaev, I. 1999, A&A, 343, 519
Mashonkina, L., Korn, A. J., & Przybilla, N. 2007, A&A, 461, 261
Meléndez, J. & Ramírez, I. 2004, ApJ, 615, L33
Michaud, G., Fontaine, G., & Beaudet, G. 1984, ApJ, 282, 206
Momany, Y., Cassisi, S., Piotto, G., et al. 2003, A&A, 407, 303
Monaco, L., Bonifacio, P., Sbordone, L., Villanova, S., & Pancino, E. 2010, Astronomy & Astrophysics, 519, L3
Monaco, L., Villanova, S., Bonifacio, P., et al. 2012, A&A, 539, A157
Monelli, M., Milone, A. P., Stetson, P. B., et al. 2013, MNRAS, 431, 2126
Mucciarelli, A., Salaris, M., & Bonifacio, P. 2012, MNRAS, 419, 2195
Mucciarelli, A., Salaris, M., Bonifacio, P., Monaco, L., & Villanova, S. 2014, Monthly Notices of the Royal Astronomical Society, 444, 1812
Mucciarelli, A., Salaris, M., Lovisi, L., et al. 2011, MNRAS, 412, 81
Nollett, K. M. & Steigman, G. 2014, Phys. Rev. D, 89, 083508
Nordlander, T., Amarsi, A. M., Lind, K., et al. 2017, Astronomy & Astrophysics, 597, A6
Nordlander, T., Korn, A. J., Richard, O., & Lind, K. 2012, ApJ, 753, 48
Osorio, Y. & Barklem, P. S. 2016, Astronomy and Astrophysics, 586, A120
Osorio, Y., Barklem, P. S., Lind, K., et al. 2015, Astronomy & Astrophysics, 579, A53
Pasquini, L., Alonso, J., Avila, G., et al. 2003, in Society of Photo-Optical Instrumentation Engineers (SPIE) Conference Series, Vol. 4841, Society of Photo-Optical Instrumentation Engineers (SPIE) Conference Series, ed. M. Iye & A. F. M. Moorwood, 1682–1693
Piau, L., Beers, T. C., Balsara, D. S., et al. 2006, ApJ, 653, 300
Piskunov, N. & Valenti, J. A. 2016, ArXiv e-prints, 1606, arXiv:1606.06073
Piskunov, N. E., Kupka, F., Ryabchikova, T. A., Weiss, W. W., & Jeffery, C. S. 1995, A&AS, 112, 525
Prantzos, N. 2006, ArXiv Astrophysics e-prints: 0612633
Prantzos, N. 2012, A&A, 542, A67
Press, W. H., Teukolsky, S. A., Vetterling, W. T., & Flannery, B. P. 1992, Numerical recipes in FORTRAN. The art of scientific computing
Proffitt, C. R. & Michaud, G. 1991, ApJ, 380, 238
Ramírez, I. & Meléndez, J. 2005, ApJ, 626, 465
Richard, O., Michaud, G., & Richer, J. 2002a, ApJ, 580, 1100
Richard, O., Michaud, G., & Richer, J. 2005, ApJ, 619, 538
Richard, O., Michaud, G., Richer, J., et al. 2002b, ApJ, 568, 979
Richer, J., Michaud, G., & Turcotte, S. 2000, ApJ, 529, 338
Royer, F., Jégouzo, I., Tajahmady, F., & Normand, J. 2012, in Astronomical Society of the Pacific Conference Series, Vol. 461, Astronomical Data Analysis Software and Systems XXI, ed. P. Ballester, D. Egret, & N. P. F. Lorente, 431
Ryan, S. G., Norris, J. E., & Beers, T. C. 1999, ApJ, 523, 654
Shi, J. R., Gehren, T., Butler, K., Mashonkina, L. I., & Zhao, G. 2008, A&A, 486, 303
Shi, J. R., Gehren, T., Zhang, H. W., Zeng, J. L., & Zhao, G. 2007, A&A, 465, 587

Sitnova, T. M., Mashonkina, L. I., & Ryabchikova, T. A. 2013, Astronomy Letters, 39, 126
Spite, F. & Spite, M. 1982, A&A, 115, 357
Spite, M., Spite, F., Gallagher, A. J., et al. 2016, arXiv:1608.03541 [astro-ph]
Takeda, Y., Zhao, G., Chen, Y.-Q., Qiu, H.-M., & Takada-Hidai, M. 2002, PASJ, 54, 275
Valenti, J. A. & Fischer, D. A. 2005, ApJS, 159, 141
Valenti, J. A. & Piskunov, N. 1996, A&AS, 118, 595
Villanova, S. & Geisler, D. 2011, A&A, 535, A31
Yong, D., Grundahl, F., Nissen, P. E., Jensen, H. R., & Lambert, D. L. 2005, A&A, 438, 875
Yong, D., Karakas, A. I., Lambert, D. L., Chieffi, A., & Limongi, M. 2008a, ApJ, 689, 1031
Yong, D., Lambert, D. L., Paulson, D. B., & Carney, B. W. 2008b, ApJ, 673, 854

Appendix A: Stellar parameters and abundances for the group averages

Table A.1. Derived elemental abundances for the coadded group-averaged spectra.

	RGB1	RGB2	RGB3	SGB1	SGB2	SGB3	TOP1	TOP2	TOP3	$\Delta \log \epsilon(X)$[a]
$T_{\rm eff}$ (K)	4747	4975	5078	5489	5642	5773	5868	5984	6212	1078
$\log g$ (cgs)	2.31	2.88	3.21	3.78	3.89	3.93	4.03	4.08	4.13	1.28
log ϵ(Li)	0.68 ± 0.05	1.05 ± 0.03	1.08 ± 0.04	1.35 ± 0.08	2.04 ± 0.03	2.09 ± 0.02	2.35 ± 0.03	2.32 ± 0.02	2.29 ± 0.02	1.43 ± 0.21
log ϵ(C)	7.23 ± 0.05	7.29 ± 0.03	7.18 ± 0.04	7.25 ± 0.06	7.10 ± 0.04	7.07 ± 0.03	7.06 ± 0.05	6.90 ± 0.03	7.02 ± 0.03	−0.24 ± 0.10
log ϵ(N)	7.63 ± 0.06	7.56 ± 0.04	7.49 ± 0.05	7.80 ± 0.08	...	...	...	...	...	...
log ϵ(O)	8.16 ± 0.04	8.13 ± 0.02	8.16 ± 0.03	8.18 ± 0.04	7.86 ± 0.04	8.02 ± 0.02	7.92 ± 0.03	7.85 ± 0.02	7.87 ± 0.02	−0.27 ± 0.04
log ϵ(Mg)	6.75 ± 0.02	6.75 ± 0.01	6.74 ± 0.02	6.71 ± 0.04	6.68 ± 0.04	6.74 ± 0.03	6.69 ± 0.06	6.71 ± 0.04	6.71 ± 0.04	−0.05 ± 0.01
log ϵ(Al)	5.77 ± 0.01	5.76 ± 0.01	5.69 ± 0.02	5.68 ± 0.04	5.59 ± 0.05	5.61 ± 0.04	5.57 ± 0.08	5.54 ± 0.06	5.54 ± 0.05	−0.19 ± 0.05
log ϵ(Si)	6.75 ± 0.02	6.73 ± 0.01	6.71 ± 0.01	6.70 ± 0.03	6.77 ± 0.03	6.72 ± 0.02	6.72 ± 0.03	6.60 ± 0.03	6.68 ± 0.02	−0.06 ± 0.06
log ϵ(K)	4.62 ± 0.02	4.63 ± 0.02	4.57 ± 0.02	4.56 ± 0.04	4.61 ± 0.04	4.62 ± 0.03	4.57 ± 0.05	4.50 ± 0.03	4.44 ± 0.03	−0.10 ± 0.08
log ϵ(Ca)	5.45 ± 0.01	5.46 ± 0.01	5.45 ± 0.01	5.40 ± 0.02	5.46 ± 0.01	5.43 ± 0.01	5.42 ± 0.02	5.38 ± 0.01	5.35 ± 0.01	−0.07 ± 0.04
log ϵ(Ti)	4.11 ± 0.03	4.10 ± 0.04	4.17 ± 0.03	4.10 ± 0.07	4.02 ± 0.08	4.06 ± 0.05	4.05 ± 0.10	3.85 ± 0.09	4.19 ± 0.06	−0.11 ± 0.09
log ϵ(Fe II)	6.24 ± 0.01	6.26 ± 0.00	6.27 ± 0.01	6.23 ± 0.01	6.31 ± 0.01	6.25 ± 0.01	6.25 ± 0.02	6.20 ± 0.01	6.20 ± 0.01	−0.07 ± 0.07
log ϵ(Ni)	5.07 ± 0.01	5.07 ± 0.01	5.06 ± 0.01	4.99 ± 0.02	5.06 ± 0.02	5.01 ± 0.01	5.04 ± 0.03	4.97 ± 0.02	4.96 ± 0.02	−0.08 ± 0.04
log ϵ(Ba)	1.43 ± 0.02	1.34 ± 0.02	1.31 ± 0.02	1.30 ± 0.04	1.25 ± 0.04	1.25 ± 0.03	1.27 ± 0.04	1.09 ± 0.03	1.11 ± 0.03	−0.20 ± 0.12
log ϵ(Eu)	−0.00 ± 0.05	−0.04 ± 0.07	−0.04 ± 0.10	< 0.30 ± 0.16	...	< −0.27 ± 0.51	< 0.22 ± 0.32	...	...	...

Notes. Abundance uncertainties are based on the statistical error as calculated by SME. Upper limits are indicated by <.
[a] The abundance difference between TOP and RGB. The TOP and RGB abundances are the averages of results for the three respective coadded group-averaged spectra. The uncertainty on the trends is based on the standard deviation of the two averages. [b] For the Li trend we did not include the coolest group-averaged abundance as it is affected by the first dredge-up.
[Li] Based on Li I λ6707.8, under NLTE. [C] Based on C I λ9111.8, under NLTE. [O] Based on O I $\lambda\lambda$7771–7775, under NLTE. [Mg] Based on Mg I $\lambda\lambda$7691.6, 7722.6 and 7811.1, under NLTE. [Al] Based on Al I $\lambda\lambda$6696–6698 and 7835–7836. [Si] Based on Si I $\lambda\lambda$7742.7 and 8892.7, under NLTE. [K] Based on K I λ7699.0. [Ca] Based on Ca I $\lambda\lambda$6462.6, 6471.7, 6493.9, 6499.7 and 6717.7, and Ca II 8912.1 and 8927.4, all under NLTE. [Ti] Based on Ti II λ6491.6. [Fe] Based on Fe II lines $\lambda\lambda$6516.1, and 7711.7, under NLTE. [Ni] Based on 12 Ni I distributed over the entire spectral range. [Ba] Based on Ba II lines λ6496.9, under NLTE. [Eu] Based on Eu II lines λ6645.1, under NLTE.